ISOTOPE SHIFT MEASUREMENTS USING K X RAYS IN Sn, Sm, and W

Thesis by

Ronald Benjamin Chesler

In Partial Fulfillment of the Requirements

For the Degree of

Doctor of Philosophy

California Institute of Technology

Pasadena, California

1967

(Submitted April 5, 1967)

ACKNOWLEDGEMENTS

The author would like to thank Dr. Felix Boehm for his essential contributions to this project. The opportunity of having worked under his guidance is greatly appreciated.

The experience of Dr. Richard T. Brockmeier in the field of isotope shifts has been of great value, and the author wishes to thank him for his important part in this work.

Thanks are also due to Mr. H. E. Henrikson, who designed the Caltech spectrometer. His work in designing the special apparatus for these experiments was invaluable. The author would also like to thank Dr. B. G. Gokhale for many valuable discussions and suggestions. The crystallographic analyses were made possible by the generous help of Dr. Sten Samson. The help of Dr. P. DuWez in connection with crystal structure modifications is also greatly appreciated. The author would also like to thank Drs. E. Seltzer and R. Hager for many interesting and valuable discussions. The assistance of Mr. Paul Lee with the data reduction and the running of the experiments deserves many thanks.

The author gratefully acknowledges financial aid from the California Institute of Technology and the U. S. Atomic Energy Commission.

Finally, the author wishes to thank his wife, Lois, for her continuing help and encouragement.

ABSTRACT

Electronic Kα1 x-ray isotope shifts have been measured for Sn 116-124, Sm 148-154, W 182-184, W 184-186, and W 182-186 using a curved crystal Cauchois spectrometer. The analysis of the measurements has included the electrostatic volume effect, screening by the transition electron as well as the non-transition electrons, normal and specific mass shifts, dynamical nuclear quadrupole polarization, and a radiative correction effect of the electron magnetic moment in the nuclear electric field. Results for the isotopic changes in the nuclear charge radii are obtained. Where other experimental data are available, the agreement with the present measurements is satisfactory. Comparisons with several nuclear model predictions yield only partial agreement.

TABLE OF CONTENTS

TABLE OF CONTENTS (Cont.)

LIST OF FIGURES

LIST OF TABLES

LIST OF ABBREVIATIONS

ABBREVIATION	MEANING
C.M.	Center of momentum
I.S.	Isotope Shift
mil	0.001 inch
mv	Milli-electron volt
M.X.U.	Milli-X-unit = 10^{-14} cm.
X.U.	X-unit = 10^{-11} cm.

I. INTRODUCTION

The variation of atomic energy levels with atomic number (Z) is well understood today. Our present understanding rests upon the firm foundation of several decades of exploration of the level systematics among the elements. Historically, these early researches formed the grand entranceway into our present structure of knowledge concerning the nature of matter. The isotope shifts (I.S.) are far more subtle and form rather a small side door not even today fully opened. The I.S. are produced when the neutron number (N) is varied, for a given Z. The shifts are in general unequal for the various atomic levels. These unequal level shifts give rise to changes in transition energies such as the x-ray I.S. which are the subject of this thesis.

There are three mechanisms through which an added neutron produces electronic level shifts. Firstly, there is the so-called volume effect, where the atomic level shifts are proportional to the changes in root mean square (rms) nuclear charge radius. The primary interaction in this case is the monopole electric force between the nucleus and the electrons. The added neutron usually "dilutes" the proton distribution, thereby decreasing its resemblance to a point charge. The atomic electrons become less tightly bound as a result. Another "volume effect" one or two orders of magnitude smaller results from the nuclear charge radius dependence of the interaction between the nuclear electric field and the radiative correction to the electron magnetic moment. The second mechanism is the "mass shift" produced by adding a neutron. This is a change in the kinetic energy of the

nuclear mass as it recoils against the motion of the electrons. The mass shift decreases in energy with increasing mass number A while the volume effect increases. The third mechanism, "dynamical nuclear polarization," comes into play when an added neutron changes the tendency of the nucleus and the electrons toward mutual deformations in shape. This effect occurs only for deformed nuclei, and is more than an order of magnitude smaller than the "volume effect."

I.S. measurements provide information on the changes in rms nuclear charge radii among isotopes of a given element. In the case of x-ray I.S., the volume effect may be accurately calculated. With the aid of a calculation of the mass shift included in the present work and an available estimate of the dynamical nuclear polarization effect, I.S. data may be interpreted to yield charge radii differences more precise than those obtained by other methods such as electron scattering experiments.

Observations of I.S. in the heavier elements (volume effect dominant) began in 1919 [1]. This and other early measurements involved shifts in optical transitions and employed standard optical interferometric techniques and unseparated isotopes. In the early 1930's, several theoretical calculations of the I.S. were carried out [2], followed by many optical I.S. measurements continuing to the present time. A recent review of the optical I.S. results has been compiled by D. N. Stacey [3]. Several researchers have contributed to the refinement of the I.S. theory and will be referred to in the pages following.

The detection of x-ray I.S. and hyperfine structure line broadening effects was attempted unsuccessfully by several workers in the period from 1931 to 1953 [4]. The I.S. was not seen because the experimental uncertainty was an order of magnitude too large. The effect of hyperfine structure on x-ray line broadening is of second order and still lies beyond experimental reach today (for electronic atoms). In 1965 Brockmeier and Boehm [5] reported the first observation of an x-ray I.S. They measured the shift of the $K\alpha_1$ x ray for the pair U 233-238 using a curved crystal DuMond spectrometer and separated isotopes. Soon afterwards, Sumbaev and Mezentsev [6,7] reported observations of x-ray I.S. for Mo 92-94-100, Nd 144-148-150, and Sm 144-150-152 using a curved crystal Cauchois spectrometer technique which was adopted also for the experiments described in this thesis.

The present measurements were carried out for the isotope pairs Sn 116-124, Sm 148-154, W 182-184, W 184-186, and W 182-186. For each pair, the shift of the $K\alpha_1$ x ray was measured. The data have been interpreted to yield the changes in the rms nuclear charge radii and the results are compared to theoretical estimates and other I.S. measurements.

With the emergence of high resolution Ge(Li) γ-ray detectors in the 1960's, x-ray I.S. and hyperfine structure observations in muonic atoms have been greatly facilitated. While current muonic I.S. results are somewhat less precise than those of the present work, there is potentially more information contained in muonic experiments owing to the greater nuclear penetration of the muonic states. Much work is currently in progress in the attempt to improve the muonic experimental

and theoretical techniques in order to realize the full potential of the field [8]. Similarly there are hopes of improving the electronic x-ray I.S. technique to allow the precise measurement of even the small single-neutron shifts.

II. THE ISOTOPE SHIFT AS A NUCLEAR PROBE

A. Introduction

Isotope shifts are changes in atomic transition energies between atoms whose nuclei have the same charge but different neutron number. In the heavier nuclei ($Z > 40$) the observed shift is due primarily to the change in the rms nuclear charge radius, the so-called volume effect.

The volume effect results primarily from the dependence of the atomic levels on the nuclear charge distribution through the electrostatic interaction between the nuclear and the electronic charges. In general the electrons become less tightly bound as the rms nuclear charge radius increases. The interaction between the radiative correction to the electron magnetic moment and the nuclear electric field is also volume dependent. In the case of nuclei whose quadrupole deformations vary greatly from one isotope to another, electric quadrupole interactions constitute a small correction to the monopole term. The interaction producing the volume effect is understood, and the electronic wave functions for at least the inner electrons are capable of accurate calculation. Therefore, observation of the I.S. can yield information concerning the change in nuclear charge radius with neutron number.

A mass shift is associated with the change in the kinetic energy of the nucleus with neutron number in the atomic C.M. system. Part of the mass shift may be simply accounted for by replacing the electron mass by its reduced mass in the Schroedinger equation. In

many electron atoms there is an additional term which has been evaluated for the cases of interest here.

As described in the next subsection, the I.S. is largest for a transition between levels of greatly differing nuclear penetration. This is the reason for choosing the Kα1 x ray (LIII → K) in preference to other x rays in the present experiments. An advantage of x-ray I.S. measurements over optical I.S. measurements lies in the possibility of calculating the relevant wave functions in the region of the nucleus much more accurately. Screening corrections are an important source of uncertainty in the case of optical I.S. evaluations.

B. The Volume Effect

An early calculation of x-ray I.S. was carried out by Wertheim [9]. He used first-order perturbation theory with relativistic Coulomb wave functions as a basis and the difference between the potentials of a point charge and a finite nuclear charge distribution as the perturbation. Because the perturbation energy is not small near r = 0, the perturbation calculation is not very accurate, and Wertheim therefore applied approximate and sizeable corrections to his results.

A more accurate method of calculation due to Broch [10] does not use perturbation theory, but uses the difference of the radial Dirac equations for the electrons of two isotopes to obtain an expression for the I.S. The method is described in detail by Bodmer,[11] who calculates numerical shifts for optical levels only however. Babushkin [12] has used the Broch method to calculate I.S. for x-ray levels. The wave functions [13] used by Babushkin were obtained by the

Sommerfeld method [14], solutions being sought inside and outside the nucleus in terms of combinations of regular and irregular Coulomb functions. Screening of the K level was taken into account using Slater's rule [15], and amounts to only a few percent.

The basic expression for the level shifts due to the finite nuclear size is given by Babushkin as

$$\Delta E = \pi\, cR^2 \left[g_o(R)\, f_e(R) - g_e(R)\, f_o(R) \right].$$

R is the "nuclear radius," $g_o(R)$ and $f_o(R)$ are the relativistic K Coulomb wave function components evaluated at R, and $g_e(R)$ and $f_e(R)$ are the finite nuclear size K wave function components evaluated at R.

The shift of the LIII level is neglected in comparison to that of the K level in these calculations. Wertheim [9] estimated the contribution to the I.S. from an LII electron to be on the order of 1% of that from a K electron for Z in the region of Sn, Sm, and W. The contribution of an LIII electron is in turn at least an order of magnitude smaller than that of an LII electron because of the vanishing LIII density at the nucleus. The neglect of the LIII shift would therefore appear to contribute no significant error.

Babushkin finds the I.S. proportional to $\delta R/R$ where δR is the isotopic change in R. As discussed below, the K shell electron density is largely constant over the extent of the nucleus. This leads to an approximate result that the I.S. depends only on the rms charge radii of the nuclei. We may without significant loss of precision take R to be the equivalent radius of a uniform charge distribution with the same rms charge radius as the actual nucleus in question: $R = \sqrt{5/3} R_{rms}$. The I.S. provides information on $\delta R/R$.

An insight into the dependence of the I.S. on the various moments of the nuclear charge distribution may be gained as follows. Consider a first order perturbation expression for the I.S. where the perturbation is the electrostatic interaction between the change in the nuclear charge density between two isotopes, and the K electron density ρ_e. For a spherical nucleus,

$$\delta(\Delta E) = 16\ \pi^2\ e^2 \int_o^\infty dr_N\ r_N^2\ \delta\rho(r_N) \int_{r_N}^\infty \frac{dr}{r^2} \int_o^r dr_e\ r_e^2\ \rho_e\ (r_e).$$

Assuming a nuclear density cutoff at R we have

$$\delta(\Delta E) = 16\ \pi^2\ e^2 \int_o^R dr_N\ r_N^2\ \delta\rho(r_N) \int_{r_N}^R \frac{dr}{r^2} \int_o^r dr_e\ r_e^2\ \rho_e\ (r_e).$$

If we expand ρ_e inside the nucleus in the form

$$\rho_e\ (r\ ) = -\frac{e}{s^3}\left(a + b\ \frac{r^2}{r_o^2} + c\ \frac{r^4}{r_o^4}\right) \qquad \text{II.1}$$

where r_o and s are dimensional constants, we get by substitution

$$\delta(\Delta E) = \frac{-16\ \pi^2 e^2}{s^3} \int_o^\infty dr_N\ r_N^2\ \delta\rho(r_N) \int_{r_N}^R \frac{dr}{r^2} \left(\frac{ar^3}{3} + \frac{br^5}{5r_o^2} + \frac{cr^7}{7r_o^4}\right)$$

and finally

$$\delta(\Delta E) = \frac{4\pi Z e^2}{s^3} \left[\ \frac{a}{6}\ \delta\langle r_N^2\rangle + \frac{b}{20}\ \delta\frac{\langle r_N^4\rangle}{r_o^2} + \frac{c}{42}\ \delta\frac{\langle r_N^6\rangle}{r_o^4}\ \right]. \qquad \text{II.2}$$

A relativistic calculation of the electronic K wave function parameters of (II.1) after the method described by Rose [16] for the case Z = 62 and A = 151 yields the result

$$\delta(\Delta E) = \frac{124\ \pi Z e^2}{3}\ \psi^2(0)\left[\ \delta\langle r_N^2\rangle + 0.033\ \delta\frac{\langle r_N^4\rangle}{r_o^2} + 0.004\ \delta\frac{\langle r_N^6\rangle}{r_o^4}\right] \quad \text{II.3}$$

where r_o has the value $1.2 \times 10^{-13}(151)^{1/3}$ cm. and $\psi^2(0)$ is the (single) K electron density at the nucleus. The relative size of the three terms of the expansion above may be readily estimated for the case of a uniform nuclear charge distribution to be 1/0.047/0.007. Higher order terms are expected to become progressively smaller. These results show that, allowing for an experimental uncertainty of a few percent, one can meaningfully interpret the I.S. as an effect of the mean square radius only. In this case the coefficient of $\delta\langle r_N^2\rangle$ in (II.3) would be readjusted slightly to partly compensate for the omission of the $\delta\langle r_N^4\rangle$ term.

For non-spherical nuclei, the equivalent radius R varies with the deformation for constant nuclear volume. Fradkin [17] shows that

$$R^2 = \bar{R}^2\left[1 + \frac{5\beta^2}{4\pi} + O(\beta^3)\right]$$

where β and $\bar{R}$ may be defined by

$$R_N(\theta,\phi) = \bar{R}\left[1 + \beta\, Y_2^o(\theta,\phi)\right]$$

for axially symmetric deformations. $R_N(\theta,\phi)$ describes a surface of

constant nuclear density. The x-ray I.S. calculated by Babushkin [12], which will be employed to extract the nuclear data from the present experiments, have taken this effect of deformation into account up to second order in β. A later investigation by Babushkin [18] shows that including terms of order β^3 and non-axial deformations does not alter the calculated shifts to a significant extent.

From Equations (II.1), (II.2), and(II.3) it can be seen that with neglect of the small variation of the electronic density over the nuclear extent, the I.S. is proportional to the K electron charge density at the nucleus. What we really have written down is the K level shift, not the isotope shift. But the LIII shift may be expressed similarly and may be neglected because of the very small penetration of an LIII electron into the nucleus. The important point is that the I.S. is proportional to the change in electron density at the nucleus. In this respect the isotope shift is similar to the isomer shift as pointed out by Reiner and Wilets [19]. The significance of this point was recognized by Wertheim [9], who included the effects of changes in the nuclear penetration of the electrons not involved in the fluorescence transition due to the change in screening between a K hole and an LIII hole. One should include these small penetration changes because the I.S. depends on the total change in the electron density at the nucleus; it reflects a shift of the atomic system as a whole.

The contribution of the K electron not involved in the $K\alpha_1$ transition may be estimated by ascribing all of its screening to the other K electron. In the case of Z = 50 this screening produces a 2%

decrease in the density at the nucleus [9]. Thus the K electron not involved in the transition decreases the I.S. by about 2%. For the two LI electrons we find (Z = 50) the electronic screening decreases nuclear penetration by a factor 0.88. Ascribing all of the screening to the K shell and taking the penetration at $\approx 1/6$ that of the K shell [20], we get a contribution $-12 \times 2 \times 1/6 \times 1/2 = -2\%$, where the factor 1/2 arises becauses only half the K shell changes in the $K\alpha 1$ transition. The contributions of other electrons may be neglected because their nuclear penetration is smaller and it changes by a relatively smaller amount since these electrons (except for LII) tend to lie outside the distributions of both levels involved in the $K\alpha 1$ transition. The results of these corrections are given in Table 1.

Another type of volume effect must also be taken into consideration. The interaction between the nuclear electric field and the radiative correction to the electron magnetic moment depends on the rms nuclear charge radius. The effect has been estimated by Breit and Clendenin [21] to contribute to the I.S. in the ratio

$$- \frac{Z\alpha(2\rho + 1)(2\rho + 3)}{8\pi r_o(\rho + 1)}$$

to the electrostatic volume effect previously discussed where

$$\rho = \sqrt{1 - (Z\alpha)^2}$$

and $r_o = 1.2 \times 10^{-13} A^{1/3}$ cm. This contribution is included in the interpretation of the I.S. data in Section VI.

TABLE 1

Corrections to the Calculated I.S. Due to Contributions by Non-transition Electrons

Z	Screened Penetration		Correction to I.S. (%)		
	K	L_1	K	L_1	Total
42	0.98	0.86	2	2	4
50	0.98	0.88	2	2	4
62	0.985	0.91	1.5	1.5	3
74	0.99	0.925	1	1	2
92	0.99	0.94	1	1	2

It is convenient to adopt a standard I.S. for purposes of communication. This standard shift is that which would be produced if the equivalent nuclear charge radius were given by $R = 1.2 \times 10^{-13} A^{1/3}$ cm. In this case

$$\frac{\delta R}{R} = \frac{\delta A}{3A} .$$

The values $\delta (\Delta E)_B$ of this standard I.S. calculated by Babushkin [12] are given in Column 2 of Table 2. The correction factors to be applied to $\delta (\Delta E)_B$ for the changes in the screening of the electrons not involved in the transition appear in Column 3. In Column 4 are the correction factors for the electron magnetic moment interaction.

C. Nuclear Polarization

In strongly deformed nuclei there is expected to be a dynamical quadrupole interaction between the nucleus and the atomic electrons. When this interaction is present to a different degree in two isotopes being compared, such as in the case of Sm 148-154, the dynamical quadrupole interaction will contribute to the observed I.S.

Reiner and Wilets [19] have calculated this energy shift by using second order perturbation theory. The qualitative picture is that the atomic K shell becomes slightly distorted by the admixture of d-states and the spin zero nucleus also admixes d-states. This may be viewed partly as a correlation between the motion of the K electrons and the orientation of the nuclear quadrupole moment which results in a slight decrease in the energy of the atomic system.

Since the quadrupole moment is proportional to the deformation parameter β, a second order perturbation calculation results in a shift proportional to $\delta (\beta^2)$. The static effect

TABLE 2

Calculated Isotope Shifts

1	2	3	4	5	6
Isotope Pair	$\delta(\Delta E)_B$ (mv)	CORRECTION FACTORS			$\delta(\Delta E)_{std}$ (mv)
		Contributions by non-transition electrons	Magnetic moment interaction	Nuclear polarization	
Sn 116-124	76.9	0.96	0.944	1	69.7
Sm 148-154	177.0	0.97	0.942	0.980	158.4
W 182-184	152	0.98	0.937	1.015	141.7
W 184-186	151	0.98	0.937	1.002	138.9
W 182-186	303	0.98	0.937	1.008	280.6

of the deformation previously mentioned is also proportional to $\delta(\beta^2)$, and Reiner and Wilets have expressed their results as a ratio of the two effects. Their result is

$$\frac{\delta(\Delta E)_{pol}}{\delta(\Delta E)_{def}} = -\frac{Z\,\alpha}{4\,\pi} = \frac{-Z}{1722}$$

which indicates that the effect of the polarization shift is to decrease the deformation contribution to the I.S. by a few percent. Using the intrinsic deformations listed by Babushkin [13] we arrive at the correction factors for the polarization effect shown in Column 5 of Table 2. The values of $\delta(\Delta E)_{std}$ obtained by applying the correction factors to Column 2 are given in Column 6.

D. Mass Shifts

The variation of nuclear mass from one isotope to another is responsible for part of the observed I.S. The mass shift contribution dominates the total shift for light elements, while for Sn(Z = 50) the mass shift is a few times smaller than the volume shift and becomes relatively less important with increasing nuclear mass.

In the center of momentum coordinate system of an atom, the total kinetic energy T may be approximated by the nonrelativistic expression.

$$T = \sum_{i=1}^{Z} \vec{P}_i^2/2m + \left(\sum_{i=1}^{Z} \vec{P}_i\right)^2/2M$$

where $\vec{P}_i$ is the momentum of the i^{th} electron, m is the electron mass and M the nuclear mass. The second term represents the recoil of the nucleus to the net electronic momentum as seen in the center of momen-

tum system of electrons plus nucleus. If we extract the cross product from the second term we have

$$T = \sum_{i=1}^{Z} \left[\frac{\vec{P}_i^2}{2m} + \frac{\vec{P}_i^2}{2M} \right] + \sum_{\substack{i=1 \\ j=1 \\ i \neq j}}^{Z} \frac{\vec{P}_i \cdot \vec{P}_j}{2M} = \sum_{i=1}^{Z} \frac{\vec{P}_i^2}{2\mu} + \sum_{\substack{i=1 \\ j=1 \\ i>j}}^{Z} \frac{\vec{P}_i \cdot \vec{P}_j}{M}$$

where $\mu = \frac{mM}{M+m}$

is the reduced electron mass. The first term above (the only one present for single electron atoms) accounts for what is well known as the "normal mass shift." Its effect is to require that the electron mass be replaced by its reduced mass in the Schroedinger equation and in the approximation that spin orbit forces are neglected in comparison to Coulomb forces, this replacement results in a linear contraction of the spectrum of the form $E(\mu) = \frac{\mu}{m} E(m)$ as shown for example by Hughes and Eckart [22].

The cross term above accounts for what is known as the Hughes-Eckart effect [22] or the "specific mass shift." Its effect has been calculated in first order perturbation theory in the present work for the Kα1 transition for Z = 42, 50, 62, and 74 using the radial wave functions of Herman and Skillman [23]. The details of the calculation are as described in an earlier calculation of this effect by Vinti [24] for several transitions in Mg. The method is outlined below.

Let the specific mass shift term be represented by σ :

$$\sigma = \sum_{i>j} \frac{\vec{P}_i \cdot \vec{P}_j}{M}$$

If U represents the determinantal wave function of the unexcited atomic electrons, we may express the specific mass shift of the Kα1 x ray by

$$\Delta E_\sigma = \langle U | \sigma_{2p} | U \rangle - \langle U | \sigma_{1s} | U \rangle$$

where $$\sigma_{2p} = \sum_{j \neq 2p} \frac{\vec{P}_{2p} \cdot \vec{P}_j}{M}$$

and similarly for σ_{1s}. These operators are sums over the pairs involving the 2p or 1s orbitals involved in the Kα1 transition. Because we are interested only in the difference in the shifts of the levels 2p and 1s we need not use the operator σ which is summed over all pairs of electrons. The observable contribution of the specific mass shift is given by

$$\delta(\Delta E_\sigma) = (\Delta E_\sigma)_A - (\Delta E_\sigma)_{A + \delta A}$$

where A and A + δA are the mass numbers of the isotopes being compared.

The wave function for the ρ^{th} orbit may be expressed as a product of space times spin $\varphi_\rho(r, \theta, \phi)\, \chi_\rho(\sigma_z)$. The functions φ and χ form orthonormal sets. Then since

$$\langle \varphi_\mu | \vec{P} | \varphi_\nu \rangle = 0$$

unless $\ell_\mu - \ell_\nu = \pm 1$, we have [25]

$$\langle U \left| \sigma_{2p} \right| U \rangle = M^{-1} \sum_{\substack{\mu=1 \\ \mu \neq 2p}}^{Z} \left| \langle \varphi_\mu \left| \vec{P} \right| \varphi_{2p} \rangle \right|^2 \vartheta_{\mu,2p}$$

where the sum over μ runs over s and d states only and $\vartheta_{\mu,2p}$ is a Kronecker delta on the spins. The matrix element of σ_{1s} may be similarly expressed and will involve a sum over p states. The formulae for the matrix elements $\langle \varphi_\mu \left| \vec{P} \right| \varphi_\upsilon \rangle$ have been worked out by Vinti [24] in the forms

$$\left| \langle n, \ell, m_\ell \left| \vec{P} \right| n', \ell-1, m_\ell \rangle \right|^2 = C_\ell^2 \left(\ell^2 - m_\ell^2 \right) F^2 (n, \ell ; n', \ell-1) \quad \text{and}$$

$$\left| \langle n, \ell\ m_\ell \left| \vec{P} \right| n', \ell-1,\ m_\ell \mp 1 \rangle \right|^2 = [1/2] C_\ell^2 (\ell \pm m_\ell - 1)(\ell \pm m_\ell) F^2(n, \ell ; n', \ell-1)$$

where

$$C_\ell = \left[(2\ell+1)\ (2\ell-1) \right]^{-1/2}$$

and

$$F(n, \ell ; n', \ell-1) = \hbar \int_0^\infty R(n\ \ell) \left\{ dR(n', \ell-1)/dr - \left[(\ell-1)/r \right] R(n', \ell-1) \right\} r^2 dr,$$

$R(n\ \ell)$ being the radial function for the orbital $n\ell$ with normalization

$$\int R^2 r^2 dr = 1.$$

This evaluation is valid only in the absence of configuration interaction. In the situation of present interest, we have only a single hole in the inner shells (K or LIII), which allows no alternative coupling possibilities for the shells. For the outer shells where configuration interaction occurs, the effect can be neglected because of the small radial overlap of these electrons with those in the K and

LIII shells. It was found for the cases Z = 42, 50, 62 and 74 considered here that the contribution of the outer electrons was small enough so that calculations made with a Pd(Z = 48) electron configuration were in error by less than 1% by neglecting the actual outer electron configurations.

Making the approximation that all the electrons in a given atom move in the same central field (an approximation used in obtaining the radial wave functions) [23] the radial integral may be cast in the form which was numerically evaluated:

$$F(n,\ell;n',\ell-1) = (2mRy)^{1/2}\left(1/2\right)\left(E(n',\ell-1) - E(n\ell)\right)\int_0^\infty R(n\ell)R(n',\ell-1)\, r^3 dr,$$

where the Ry is the Ryderg energy, m the electron mass, and E the (negative) electronic level energy. The unit of r is the Bohr radius.

The results of the calculations are given in Table 3 and Figure 1 along with the normal mass shifts for comparison. The observable shift is obtained from the plotted $A\,\Delta E$ according to the formula $\delta(\Delta E)_M = \bar{A}\,\Delta E \times \frac{\delta A}{\bar{A}^2}$ where $\bar{A}$ is the average mass number of the isotope pair. The specific mass shift is approximately -1/3 times the normal mass shift for the range of Z considered. The results for the specific mass shift are expected to be accurate to better than 10%, the error stemming largely from the approximate radial functions. Relativistic corrections should not be important since the next order relativistic correction to the perturbing operator is of the form

TABLE 3

Normal and Specific Mass Shifts of the $K\alpha 1$ X Ray

Isotope Pair	Normal Mass Shift (mv)	Specific Mass Shift (mv)	Total Mass Shift (mv)
Mo 92-100	-8.28	+2.76	-5.52
Sn 116-124	-7.65	+2.52	-5.13
Sm 148-154	-5.75	+1.87	-3.88
W 182-184	-1.93	+0.61	-1.32
W 184-186	-1.89	+0.60	-1.29
W 182-186	-3.82	+1.21	-2.61

Figure 1. Specific and normal mass shifts for the Kα1 x ray. The mass shifts are obtained from the plotted $A\Delta E$ by the formula $\delta(\Delta E)_M = (\overline{A}\,\Delta E) \times \delta A/\overline{A}^2$ where δA is the mass difference between the isotopes and $\overline{A}$ is the average mass number. The observable mass shift is the sum of the normal and specific mass shift contributions.

Figure 1

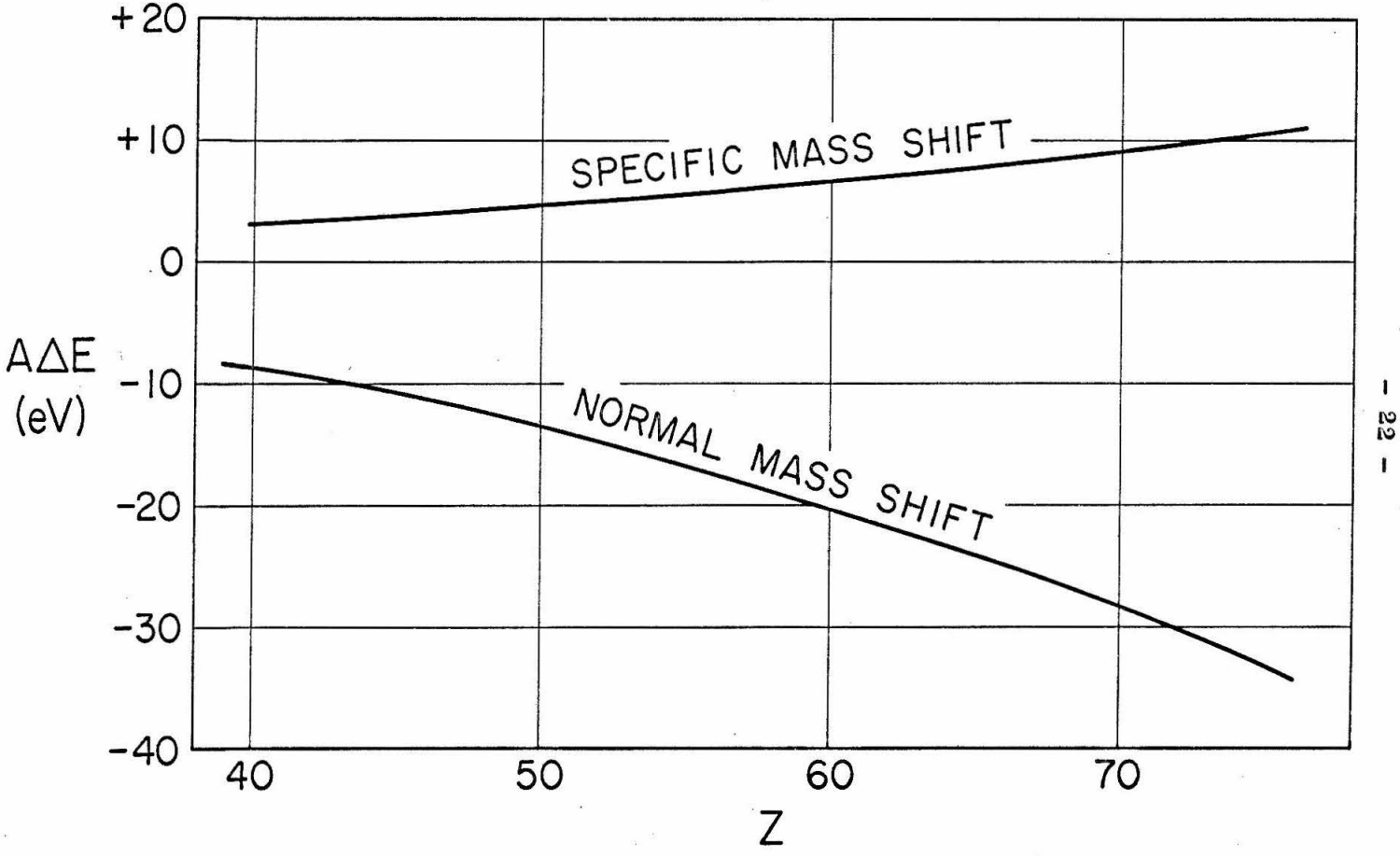
+20
+10
0
-10
-20
-30
-40
AΔE
(eV)
SPECIFIC MASS SHIFT
NORMAL MASS SHIFT
40
50
60
70
Z

$$\frac{-(\sum \vec{P}_i \cdot \vec{P}_j)^2}{8M^3 c^2}$$

which is negligibly small compared to

$$\sum \frac{\vec{P}_i \cdot \vec{P}_j}{2M}$$

because of the large nuclear mass M.

E. Small Effects

The Lamb shift contributes to the I.S. through its dependence upon the reduced electron mass. Kroll and Lamb [26] have given an expression for the Lamb shift of the K level (including vacuum polarization):

$$\Delta E_k = 8 \frac{\alpha^3 Z^4}{3\pi} (Ry)_A \left(\ln \frac{M}{K_o} - \ln 2 + \frac{5}{6} - \frac{1}{5}\right) \qquad (II.4)$$

where $(Ry)_A$ is the Rydberg energy with reduced mass appropriate to a nucleus of mass number A, and K_o is an average excitation energy of the atom, approximated here by the Kα1 x-ray energy for the atom in question. We have

$$(Ry)_A = \frac{M}{M+m} \times (Ry)_\infty = \left(1 + \frac{1}{1836A}\right) (Ry)_\infty \text{ , and } \delta(Ry)_A \approx \frac{\delta A}{1836A^2} (Ry)_\infty . \qquad (II.5)$$

Using Equations (II.4) and (II.5) we obtain contributions to the Sn 116-124, Sm 148-154, and W 182-186 I.S. of 0.025 mv, 0.023 mv, and 0.018 mv, respectively. Although the Lamb shift formula (II.4) is subject to important corrections from terms of higher order in αZ, the very small shift yielded by (II.4) compared to the observed shifts

(on the order of 25 mv or larger) would seem to justify neglecting the role of the Lamb shift in the present observations.

An electron-neutron interaction reported by Havens, Rainwater, and Rabi [27] has been discussed by Wilets and Hill [28]. The ratio of the expected effect to the nuclear volume effect is predicted to be about 0.017 for Sn and less for Sm and W. However, it is possible that this effect may be absent or considerably smaller for the addition of neutron pairs as in the cases under consideration here. This effect will be neglected in the analyses of the present experiments.

The monopole counterpart to the quadrupole polarization effect discussed in the previous subsection has been estimated by Reiner and Wilets [19] and found to be several orders of magnitude smaller than the quadrupole polarization effect. Monopole polarization will therefore be ignored. The analogous dipole polarization effect is expected to be yet smaller than the monopole effect. Therefore it will also be ignored.

III. EXPERIMENTAL METHOD

A. General Description

The method used here to measure x-ray shifts was first employed by Sumbaev and Mezentzev in connection with chemical shift [29] and I.S. [6,7] experiments. This technique is well suited to the problem of measuring x-ray line shifts on the order of one-thousandth of the natural line width. These small shifts have been measured as described below with a precision of a few percent.

Excitation of the Kα1 x rays to be studied was accomplished by placing target material in the beam of bremsstrahlung x rays produced by a medical x-ray tube. The x-ray fluorescent radiation emitted by the target was analyzed by a Cauchois spectrometer programmed to scan over the region of the Kα1 x ray. A scintillation counter located behind a narrow receiving slit served as detector for the spectrometer. The wavelength comparison between samples was made by scanning over the Kα1 profile in discrete steps with the sample material being interchanged at each step of the scanning. Thus the profiles of the Kα1 x rays of both samples were traced out with each scan across the Kα1 region. The pulses from the scintillation detector were amplified, processed by a single channel differential discriminator, counted in a single channel scaler, and read out onto a card punch after each counting interval while the samples were being interchanged. The system functioned automatically with repetitive scannings of the Kα1 region. Details of the apparatus and procedure are given in following subsections. A schematic diagram of the system is shown in Figure 2.

Figure 2. Cauchois spectrometer and control system. The crystal to receiving slit distance is approximately 2 M.

Figure 2

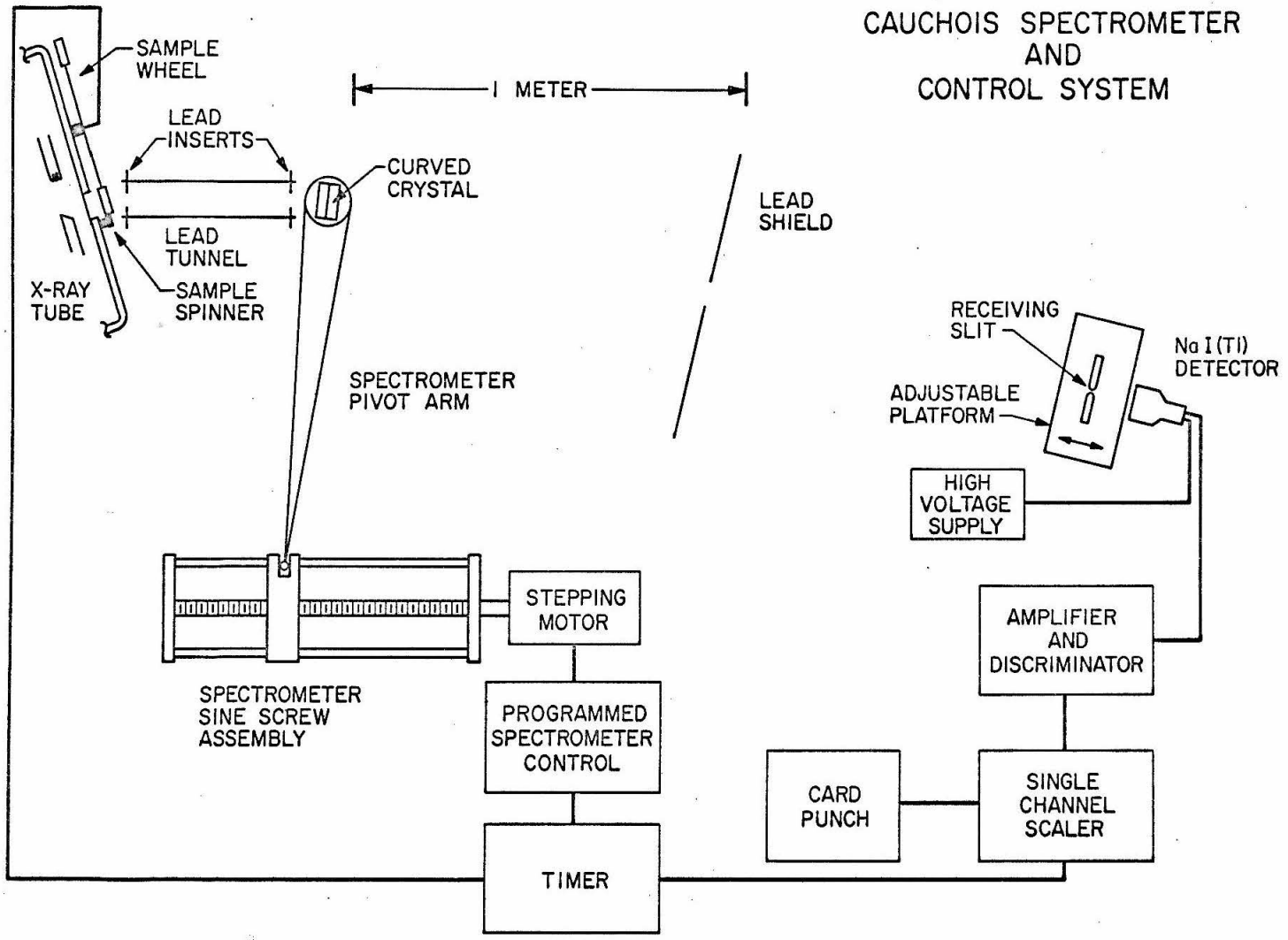
CAUCHOIS SPECTROMETER
AND
CONTROL SYSTEM
SAMPLE WHEEL
1 METER
LEAD INSERTS
CURVED CRYSTAL
LEAD SHIELD
LEAD TUNNEL
X-RAY TUBE
SAMPLE SPINNER
SPECTROMETER PIVOT ARM
RECEIVING SLIT
NaI(Tl) DETECTOR
ADJUSTABLE PLATFORM
HIGH VOLTAGE SUPPLY
STEPPING MOTOR
AMPLIFIER AND DISCRIMINATOR
SPECTROMETER SINE SCREW ASSEMBLY
PROGRAMMED SPECTROMETER CONTROL
CARD PUNCH
SINGLE CHANNEL SCALER
TIMER

Since only the shift between the wavelengths of the samples was to be measured, only one "side" of the diffraction pattern was observed in contrast to absolute wavelength measurements where both "sides" are scanned in order to establish the zero point of the wavelength scale. Also, the region of scan was sufficiently narrow to allow holding the target stationary during the scan, the diffraction crystal rotation being the only motion during the scanning of a given $K\alpha_1$ profile.

B. Excitation of the $K\alpha_1$ X Rays

Fluorescent $K\alpha_1$ transitions were excited by bombarding the target with bremsstrahlung x rays supplied by a medical-type wolfram anode x-ray tube. The target was positioned near the exit window of the x-ray tube so as to receive maximum irradiation from the tube. In order to minimize background counts and simplify shielding against stray radiation, the x-ray beam was limited to a size not much larger than the target by the insertion of a 1/4 inch thick lead diaphragm with a central circular aperture at the exit window of the x-ray tube.

The intensity of the fluorescent $K\alpha_1$ radiation depends on the operating conditions of the x-ray tube and the configuration of the target. The optimum target configuration is described in the next subsection. The intensity averaged over angles of the bremsstrahlung radiation per unit energy interval from a thick-target tube, such as that employed here, decreases approximately linearly with increasing energy:

$$dI = \text{const.} \quad (E_{max} - E)\, dE$$

where E_{max} = eV and V is the tube voltage [30]. Since each x-ray quantum carries an energy E, the corresponding dependence for the number of x rays per unit energy interval is obtained by dividing by E;

$$dN = \text{const.} \left\{ \frac{eV}{E} - 1 \right\} dE \quad .$$

This relation shows that, for given tube current, more x rays are produced at all energies as the tube voltage is increased.

In the present experiment it was desirable to maximize the number of bremsstrahlung x rays just above the K ejection threshhold. Therefore, the maximum possible tube voltage and current values of 160 Kv and about 20 ma. were used in the present experiments.

The external x-ray beam was directed at a small angle with respect to the lead tunnel shown in Figure 2 so that the portion of the beam not interacting with the target would be largely absorbed and dissipated inside the lead tunnel.

C. The Sample Configuration

Since I.S. are about a thousand times smaller than x-ray line widths, it is necessary to measure the shift between two isotopically separated samples, each one highly enriched in a particular isotope.* The isotopic compositions of the samples used in the present experiments are shown in Table 4.

*The observable effect of the I.S. for a sample containing two or more isotopes in comparable amounts would be an undetectably small increase in line width. This widening effect is of second order in the I.S. compared to the line width, whereas the shift in profile centers between two enriched samples is first order in this small ratio.

TABLE 4

Target	Mass Number	Isotopic Composition (Atomic %)
Sn 116	112	0.01
	114	0.03
	115	0.08
	116	95.60
	117	1.63
	118	1.48
	119	0.27
	120	0.63
	122	0.11
	124	0.16
Sn 124	116	0.43
	117	0.30
	118	1.17
	119	0.40
	120	1.75
	122	1.21
	124	94.74
Sm 148	144	0.1
	147	1.1
	148	95.37
	149	1.45
	150	0.45
	152	0.92
	154	0.62
Sm 154	147	0.04
	148	0.04
	149	0.19
	150	0.04
	152	0.39
	154	99.30
W 182	182	94.32
	183	2.54
	184	2.32
	186	0.82
W 184	182	1.83
	183	2.02
	184	94.22
	186	1.93
W 186	182	0.45
	183	0.33
	184	2.16
	186	97.06

The samples used were the oxides SnO_2, Sm_2O_3, and WO_3 obtained from Oak Ridge National Laboratory. Each sample of a given element was processed by ORNL according to a standardized procedure, the last step of which was to roast the material in the presence of oxygen, which would eliminate hydrated forms and oxides of lower oxidation state. The effects of possible chemical dissimilarity between samples of a given element and the steps taken to avoid error from this source are discussed in Section V.

The powdered sample was arranged to provide maximum counting rate consistent with minimizing intensity variations over the sample. These variations can couple with spectrometer aberrations to cause aberrational shifts. The spectrometer aberrations are discussed in the next subsection.

If the bremsstrahlung excitation beam were of unlimited extent and the spectrometer crystal aperture indefinitely large, then maximum intensity from a given sample would be obtained by using very thin targets to eliminate shielding of one atom by another. The spectrometer crystal was about 4x5 cm., smaller than the bremsstrahlung beam, and so places an upper limit on the useable extent of the target. The second criterion, that of minimizing relative intensity variations among the targets under comparison, leads to the choice of a definite target thickness. This is so because the excitation rays and the fluorescent rays must enter and leave on opposite sides of the target. The optimum target thickness "t" minimizes fluorescent intensity variations over the target surface due to small deviations from the average

target thickness because the slope of the intensity vs. thickness curve is zero at this point. By using μ, the absorption cross section for Kα1 fluorescent radiation just below the K edge, and by assuming a single absorption cross-section μ_1 for the exciting radiation we can express t approximately as

$$t = \frac{\ell n(\mu / \mu_1)}{\mu - \mu_1} \quad .$$

With this estimate as a starting point, the optimum thickness was determined experimentally using non-enriched samples. Results could be transferred to the enriched isotopes by measuring the density of each powder. The procedure was to set the spectrometer on the profile peak and then compare the counting rates of several samples of constant diameter and graduated thicknesses. Cylindrical lucite holders, each having a cylindrical cavity of prescribed dimensions and a loading port, were used to contain the powder. A holder is illustrated in Figure 3. The samples of graduated thickness were mounted in the sample wheel and were successively exposed to the beam for counting. The results of such an experiment for the W case are shown in Figure 4. Optimum thicknesses for isotopically natural tin, samarium, and wolfram as determined by this method are 0.0671, 0.118, and 0.175 g/cm^2 respectively. These results may be extended to other elements by means of the interpolated curve of optimum target thickness vs. Z shown in Figure 5.

The optimum thicknesses lead to target diameters of 2.5 to 3 cm. with the amounts of enriched material available. Slightly

Figure 3. Sample Holder. The lucite holder has a cylindrical cavity of the optimum thickness for the particular experiment, and a single loading port. The cavity diameter varied from 2.5 to 3.0 cm. and the cavity thickness from 13 to 69 mil for the different experiments.

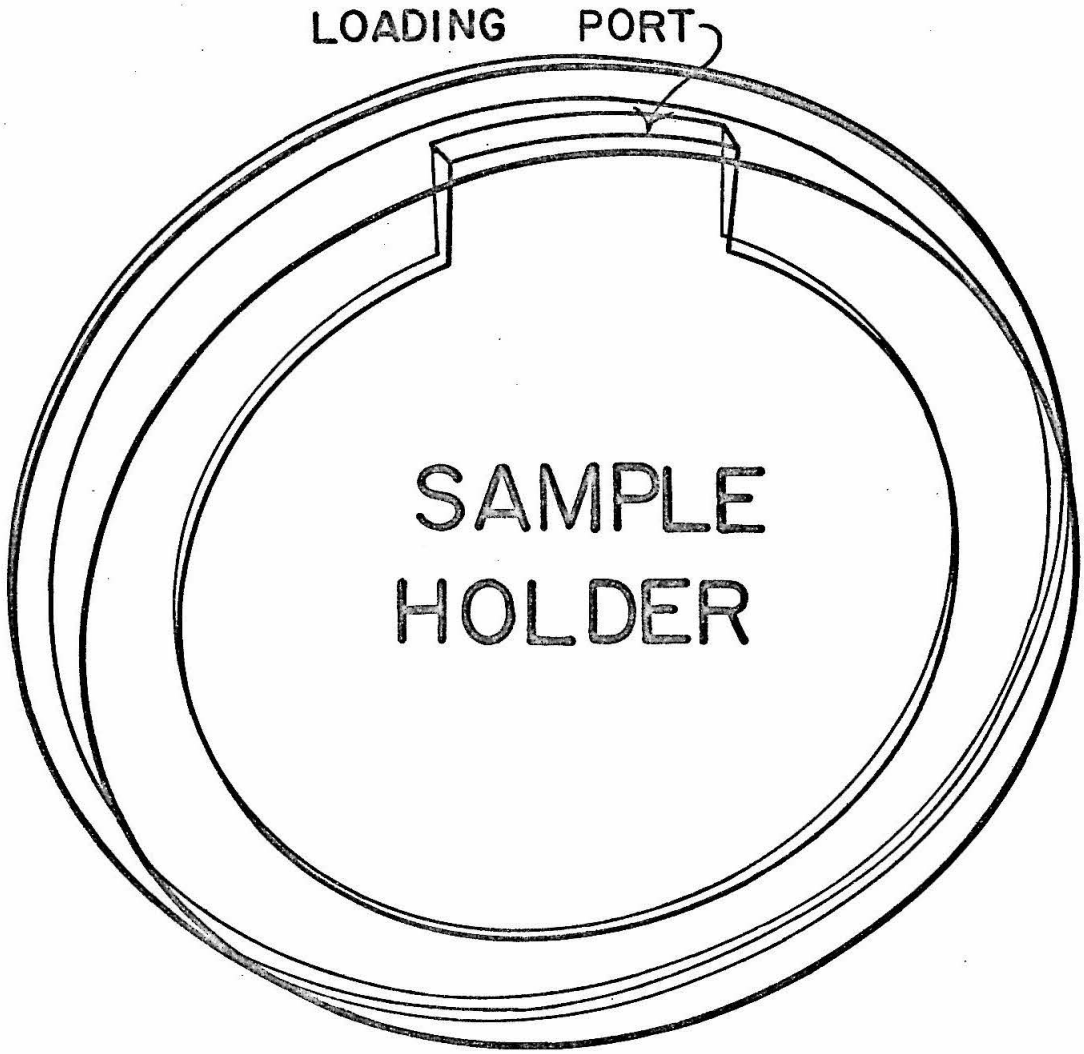

Figure 3

Figure 4. Optimum wolfram target thickness. The data points represent the counting rates for sample holders of varying cavity thickness and constant diameter with the spectrometer set at the wolfram $K\alpha_1$ peak center.

Figure 4

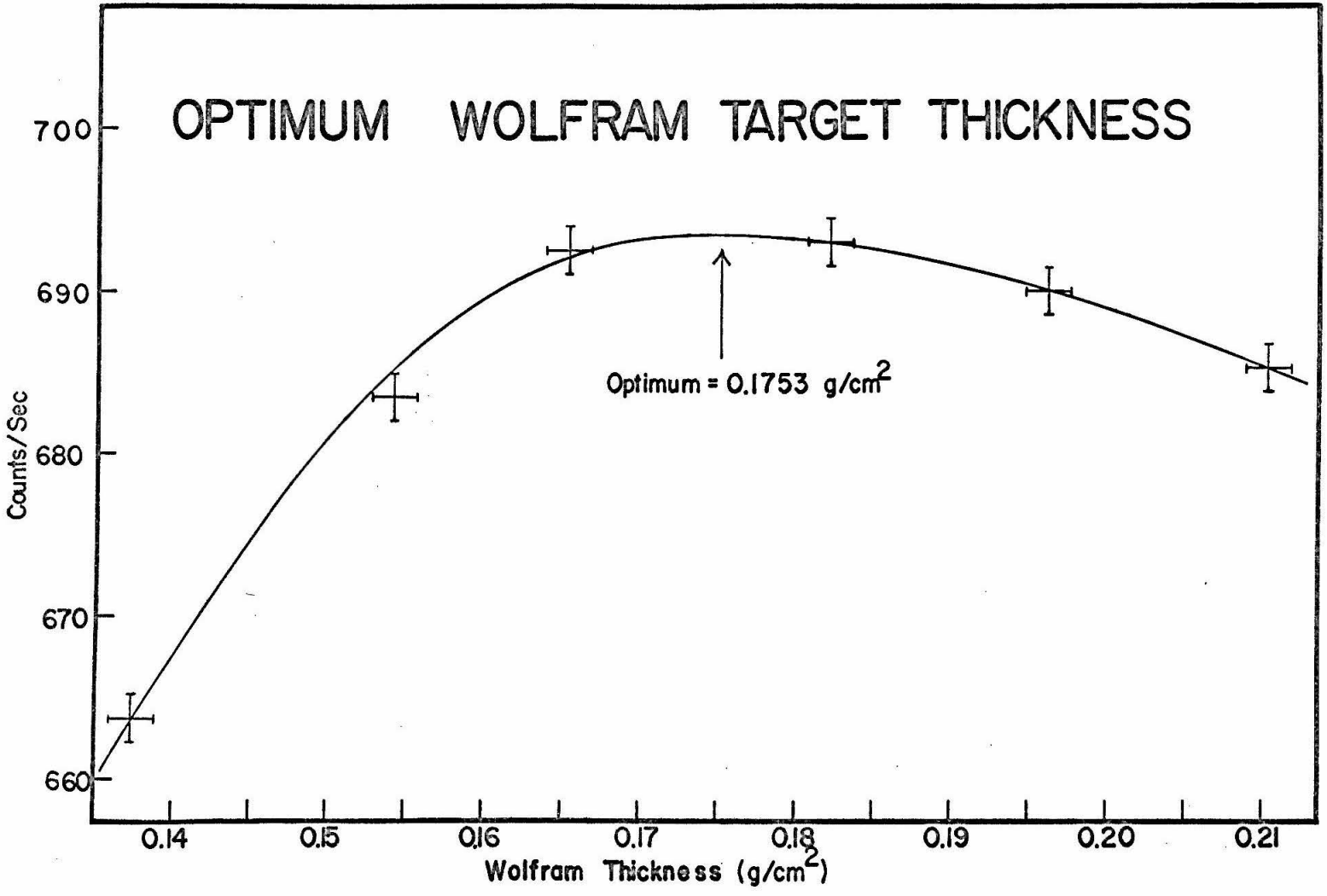
OPTIMUM WOLFRAM TARGET THICKNESS
700
690
680
670
660
Counts/Sec
Optimum = 0.1753 g/cm2
0.14
0.15
0.16
0.17
0.18
0.19
0.20
0.21
Wolfram Thickness (g/cm2)

Figure 5. Optimum target thickness vs. A. A smooth curve has been drawn between the three data points obtained by the method illustrated in Figure 4. These results apply to samples of natural isotopic composition.

Figure 5

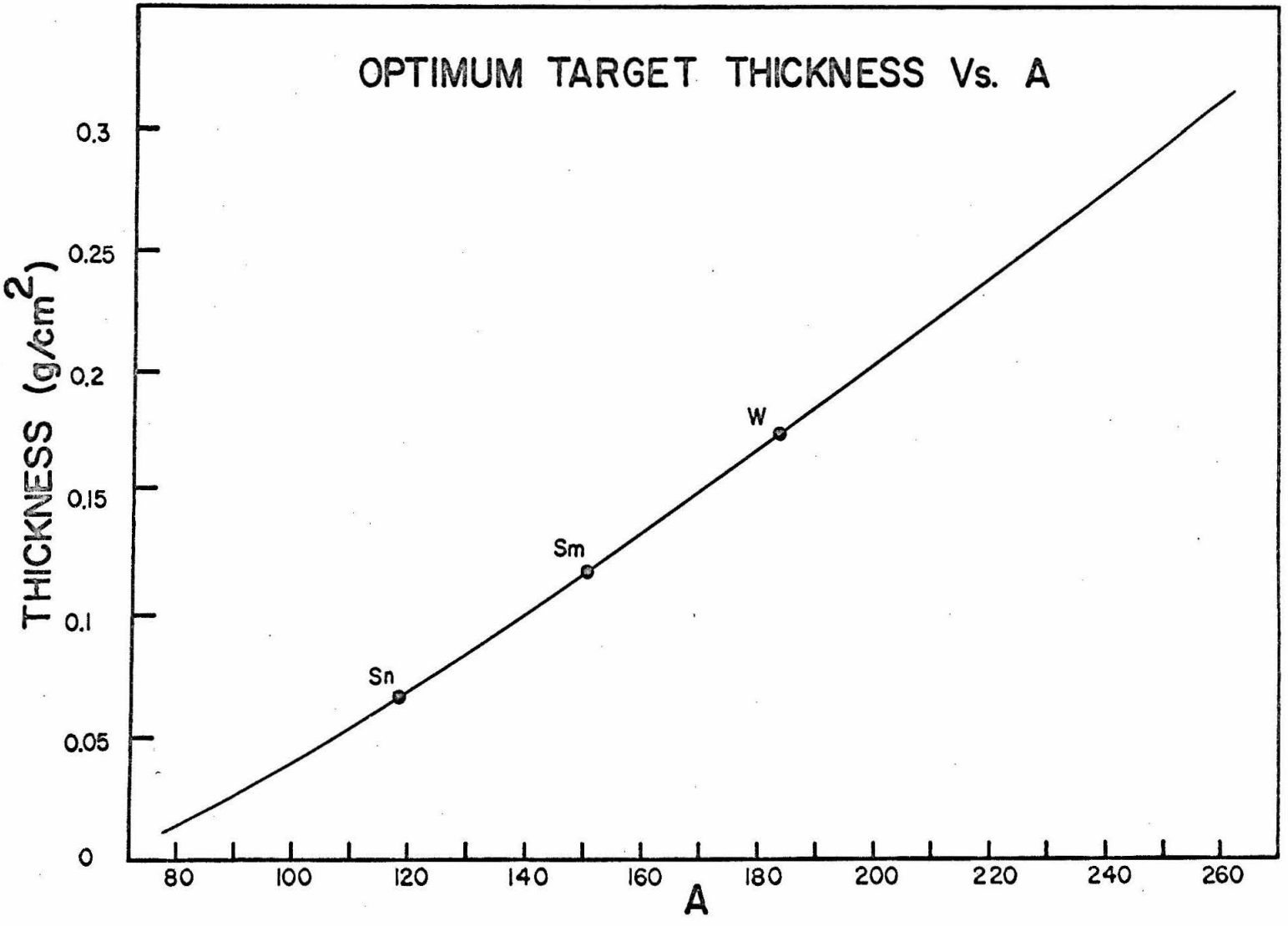
OPTIMUM TARGET THICKNESS Vs. A
THICKNESS (g/cm^2)
0.3
0.25
0.2
0.15
0.1
0.05
0
Sn
Sm
W
80
100
120
140
160
180
200
220
240
260
A

larger counting rates could have been achieved by using thinner and larger targets (as large as the crystal aperture) but this counting rate criterion was sacrificed to the more important one of eliminating relative intensity variations over the target by using the optimum thicknesses in the actual experiments. There were of course intensity variations over the target caused by the particular angular distribution of the exciting bremsstrahlung radiation, but this variation is of no concern since it is common to the two samples under comparison.

Two further steps taken to reduce fluorescent intensity variations over the sample were to grind the powder to sufficient fineness to pass through a 200 mesh sieve, and to rotate the cylindrical target about its center at about 10 rpm during the counting. The rotation has the effect of averaging the intensity over one of the two degrees of freedom of the target surface. The effects of the residual intensity variations over the samples are treated in the error discussion of Section V.

The area of the sample seen by the Cauchois spectrometer was determined by the circular aperture in the lead insert placed near the sample end of the lead tunnel shown in Figure 2. Another similar insert was placed near the crystal end of the tunnel. The latter insert served only to absorb scattered radiation. Because of the angle between the direction of the external bremsstrahlung beam (which was perpendicular to the sample plane) and the central sample-to-crystal line, the sample presented an elliptical cross-section to the spectrometer in the absence of the defining lead insert. The diameters of the lead inserts

were chosen to be about 10-15% smaller than the minor axis of this ellipse.

D. The Cauchois Spectrometer

The curved crystal spectrometer used in these experiments was designed by H. Henrikson and is described in detail elsewhere [31]. The apparatus is shown schematically in Figure 2. For use with the moderately large diffracting angles of the present experiments, a collimator consisting of a simple lead tunnel was found sufficient to block the direct beam from the detector.

The crystal pivot was attached to a sine screw mechanism. A Slo-Syn motor was mounted to step the sine screw through small, constant angular increments. Rotating the sine screw resulted in rotation of the curved crystal. Using the 310 planes of quartz for first order diffraction the smallest possible step size corresponded to an increment of 10 milli-X.U. (M.X.U.) in wavelength. The automatic spectrometer control system, described in the next subsection, allowed the basic 10 M.X.U. step to be compounded so that larger steps could be programmed when desired.

In general, the scanning of a Dumond or Cauchois spectrometer requires displacement of the source or the detector as well as rotation of the curved crystal in order to maintain the conditions for Bragg diffraction. In the present case however, the total scanning angle has an order of magnitude of only one minute of arc. The sample displacement to accompany a scan of this arc is about 0.2 mm. This small displacement was automatically taken care of in the present experiments because the curved crystal was large enough to allow the crystal area

actually in use to shift by 0.2 mm during the scanning. The only sample motion necessary was the slow rotation to reduce aberrations.

The receiving slit was positioned at the focus of the spectrometer and its width set at the optimum value for each of the elements studied. The optimum slit width is such that the observed profile width is greater than the profile width observed with a very narrow slit by the factor of approximately $\sqrt{2}$. This choice of slit width minimizes the error in the determination of the center of the profile for a given duration of measurement by minimizing the ratio of profile width to the square root of the average counting rate. If we consider the profile to have unit second moment and fold it with a rectangular step (the slit) of width W (and second moment $W^2/12$) we obtain for the convolute a second moment $1 + W^2/12$. The average counting rate is very nearly (neglecting background) proportional to W. The uncertainty therefore varies like

$$\sqrt{\frac{1 + W^2/12}{W}} \quad .$$

This function has its minimum at $W^2 = 12$, in which case the convolute has its second moment equal to twice that of the unfolded profile. Neglecting the "small" change in shape of the profile before and after folding with the rectangular step, the full width at half maximum will increase approximately by the factor $\sqrt{2}$ at the optimum slit width. Figure 6 illustrates the relative sizes of the slit and the unfolded and folded profiles under this optimum condition.

In considering aberrations of the Cauchois spectrometer it is

Figure 6. Profile broadening at optimum slit width. The unfolded and folded profiles have half-widths of 1 and $\sqrt{2}$ (arbitrary units) respectively. The slit width is 1.47 on the same arbitrary scale.

Figure 6

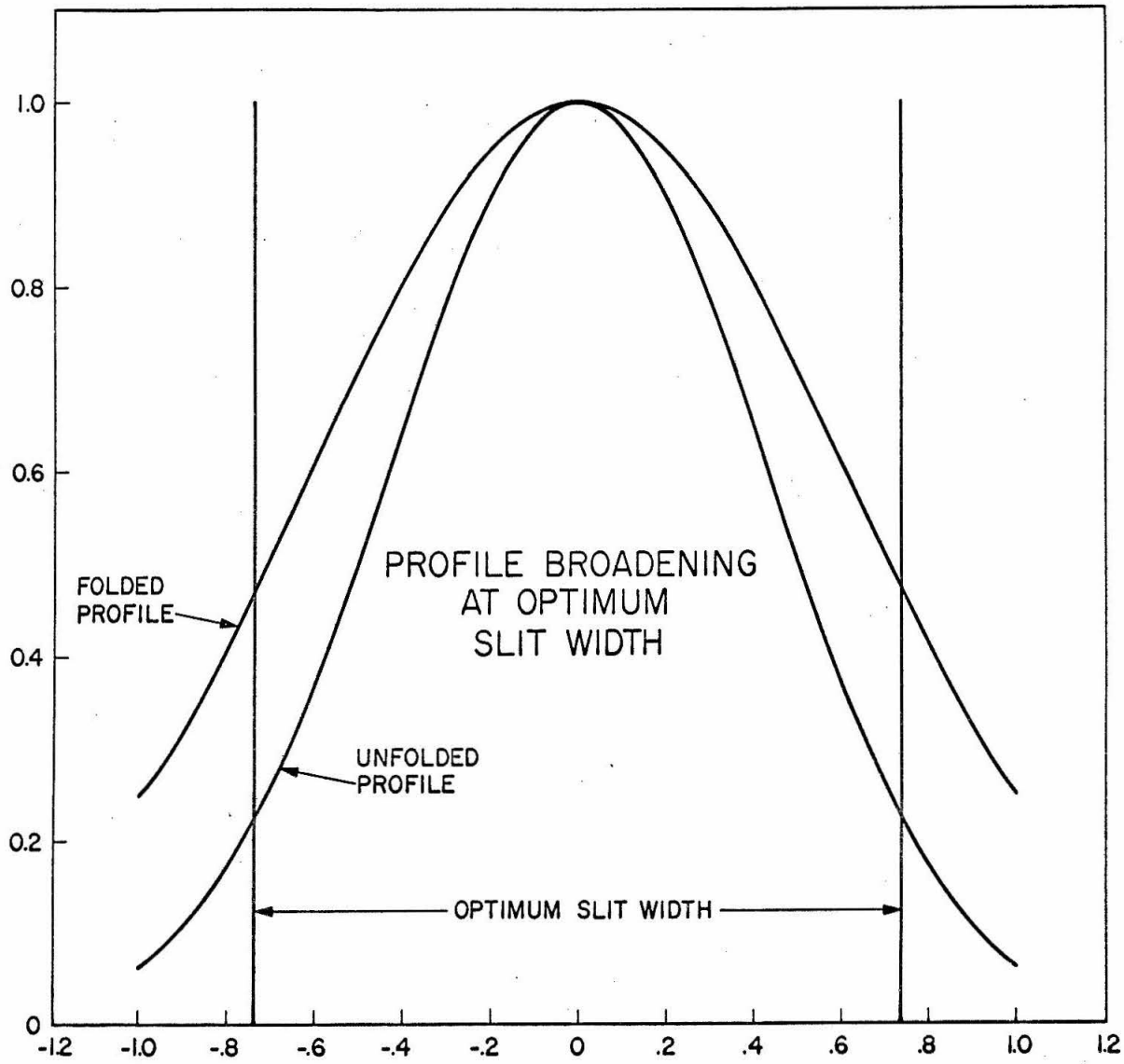
PROFILE BROADENING
AT OPTIMUM
SLIT WIDTH
FOLDED
PROFILE
UNFOLDED
PROFILE
OPTIMUM SLIT WIDTH
1.0
0.8
0.6
0.4
0.2
0
-1.2
-1.0
-.8
-.6
-.4
-.2
0
.2
.4
.6
.8
1.0
1.2

important to note that to each point on the plane of the extended sample corresponds a narrow strip about 1/60 mm. wide on the crystal where the diffraction maximum occurs. This small width corresponds to the 13 seconds of arc constituting the mosaic width of the curved crystal. As a result, each small area of the sample uses a unique area of the curved crystal to diffract its Bragg angle radiation. Now different parts of the curved crystal do not focus their Bragg diffracted rays at exactly the same point due to the vertical divergence effect (foci are circular sections, not lines), random crystal imperfections, non-uniformities in bending, and inexact location of the slit at the optimal distance from the crystal. The vertical divergence effect contributes a wavelength aberration given approximately by the formula

$$\Delta\lambda \approx \frac{\lambda s^2}{8R^2}$$

where λ is the wavelength of the diffracted radiation, s is the receiving slit height (the crystal aperture height is assumed to be of similar size) and R is the crystal-to-slit distance. For the present measurements in tin we take $\lambda \simeq 500$ X.U., $s \simeq 2$ cm., and $R \simeq 2M$. The result is

$$\Delta\lambda \approx 6 \text{ M.X.U.}$$

By experimenting with small sources located in various positions with respect to the crystal, the total variation in focal point is observed to have a standard deviation of about 10 M.X.U. Thus samples with different intensity distributions over their surfaces will show an apparent wavelength shift. By rotating the samples we effectively

remove azimuthal intensity variations, but radial variations remain. The magnitude of the systematic error introduced into the measurements by this aberration effect is discussed in Section V.

E. Spectrometer Control System

The spectrometer control system was devised by R. T. Brockmeier to allow automatic scanning of the spectrometer with variable step size and counting time. When operated in the automatic mode the spectrometer repeated indefinitely a measurement cycle consisting of a thirty-five point scan of a prescribed region, a rewind past the scan starting point, and a rapid step to the scan starting point. The rewind beyond the starting point and the uni-directional scanning eliminated problems of backlash in the sine screw and other parts of the crystal rotation mechanism.

The counting interval was the same for each of the thirty-five scan points and could be programmed for any integral number of seconds from 1 to 9999. Timing information was derived from the 60 cps line frequency. The first three and last three steps of the scan were adjustable in size from 20 to 200 M.X.U. with the 310 quartz planes in first order, and the middle 28 steps were adjustable from 10 to 100 M.X.U. under the same conditions. Using larger steps at the extremes of the scan range was more efficient than using only one step size because the extremes of the scan were essentially background measurements.

The choice of counting interval was determined by the compromise between minimizing drift errors and minimizing dead time losses

due to unnecessarily frequent sample interchanges. The sample interchange process required about 5 seconds. With the 20 second counting interval used in these experiments, counting efficiency was about 80%. Estimates of the statistical error introduced by random drifts indicated that the statistical uncertainties in the measured shift were only 10 to 20% greater than they would have been in the absence of any drifts. The error in the absence of drifts was calculated from the observed profile widths and counting rates. Maximum efficiency is obtained when the uncertainty contribution from drifts is equal to that due to readout time losses. The 20 second counting interval proved to be a reasonable choice in this respect.

In the present experiments two samples A and B were compared by placing them alternately in the bremsstrahlung beam at the source position for the spectrometer. The counting sequence used was to count A, B, A step spectrometer, count B, A, B step spectrometer, etc. Since the number 35 of counting positions over the scan is odd, the sample order alternated with each scan.

F. Detector and Readout Systems

An NaI(Tℓ) scintillation counter was used to detect the x rays passing through the receiving slit. The pulse signals were fed from the photomultiplier anode to a preamplifier and amplifier in cascade. The output pulses were then analyzed by a single channel differential discriminator adjusted to accept only the photopeak pulses. The pulses from the discriminator were stored in a single channel scaler with 10^5 count capacity. At the end of each 20 second counting interval

the scaler was automatically read out onto an IBM card punch machine and cleared. The card readout proved to be reasonably trouble-free and was convenient for data reduction by computer.

The highest counting rates encountered in these experiments were on the order of 2500 counts per second and did not approach the limits of the pulse handling capacity of the system.

IV. DATA REDUCTION

A. Introduction

Because the line shifts in these experiments were to be determined to within approximately a ten-thousandth of the profile line widths, data reduction was carried out with the aid of a computer. The general procedure was to divide the data into blocs corresponding to approximately three hours of running time. For each data bloc a least square fit was made to each of the two profiles corresponding to the two samples being compared. The data of each bloc then yielded a value for the I.S. equal to the difference between the peak center parameters of the profiles of the two samples. The values of the shifts obtained from each data bloc were then averaged. This average then represented the uncorrected I.S. value for the experiment.

The uncertainty in the measured value of the I.S. was obtained from the spread of values among the shifts obtained from the individual data blocs. All uncertainties quoted below represent the standard deviation of the mean. The data reduction procedure will be discussed in greater detail in the subsections to follow.

B. Procedure

The raw data were broken down into blocs. Each bloc contained the data from four scans across the profile. A bloc represented approximately three hours of running time and the experiments contained from seventy-seven to one hundred thirty-five such blocs. The bloc size was selected to be small enough so that a number of experimental values large enough for statistical analysis could be obtained, but large

enough to avoid requiring excessive computing time. Counts taken at given spectrometer positions were summed over the four scans comprising a data bloc. A data bloc was thus characterized by 35 numbers for each of the two samples, corresponding to the 35 point scan of the spectrometer.

A least squares program was used to make a five parameter fit to each of the two profiles of each data bloc. The fitting function consisted of a Gaussian with peak height, half width, and center position parameters plus a background with average value and slope parameters. Figure 7 shows a typical profile from one data bloc and its corresponding least squares fit. The slight systematic difference in shape between the fitting function and the data is not a source of concern in the present experiment for reasons explained in the next subsection.

The experimental value for the line shift for a single data bloc corresponded to the difference between the peak center parameters of the least square fits for the profiles of the two samples. In this way a large number of single values of the experimental shift were obtained, one value for each of the data blocs.

A second computer program written by R. T. Brockmeier averaged the shift values to obtain the final shift value for the experiment. This program also computed the uncertainty in the final value by calculating the standard deviation of the mean according to the formula

$$\sigma = \frac{\sqrt{\sum_{i=1}^{N}(x_i - \bar{x})^2}}{\sqrt{N(N-1)}} \quad .$$

Figure 7. Least squares fit to Sn Kα1 x-ray profile. The data are taken from a typical data unit bloc. The Sn Kα1 wavelength is λ = 489.57 X.U. and the half-width of the fitting profile is $\Gamma_{\frac{1}{2}}$ = 0.4014 X.U.

Figure 7

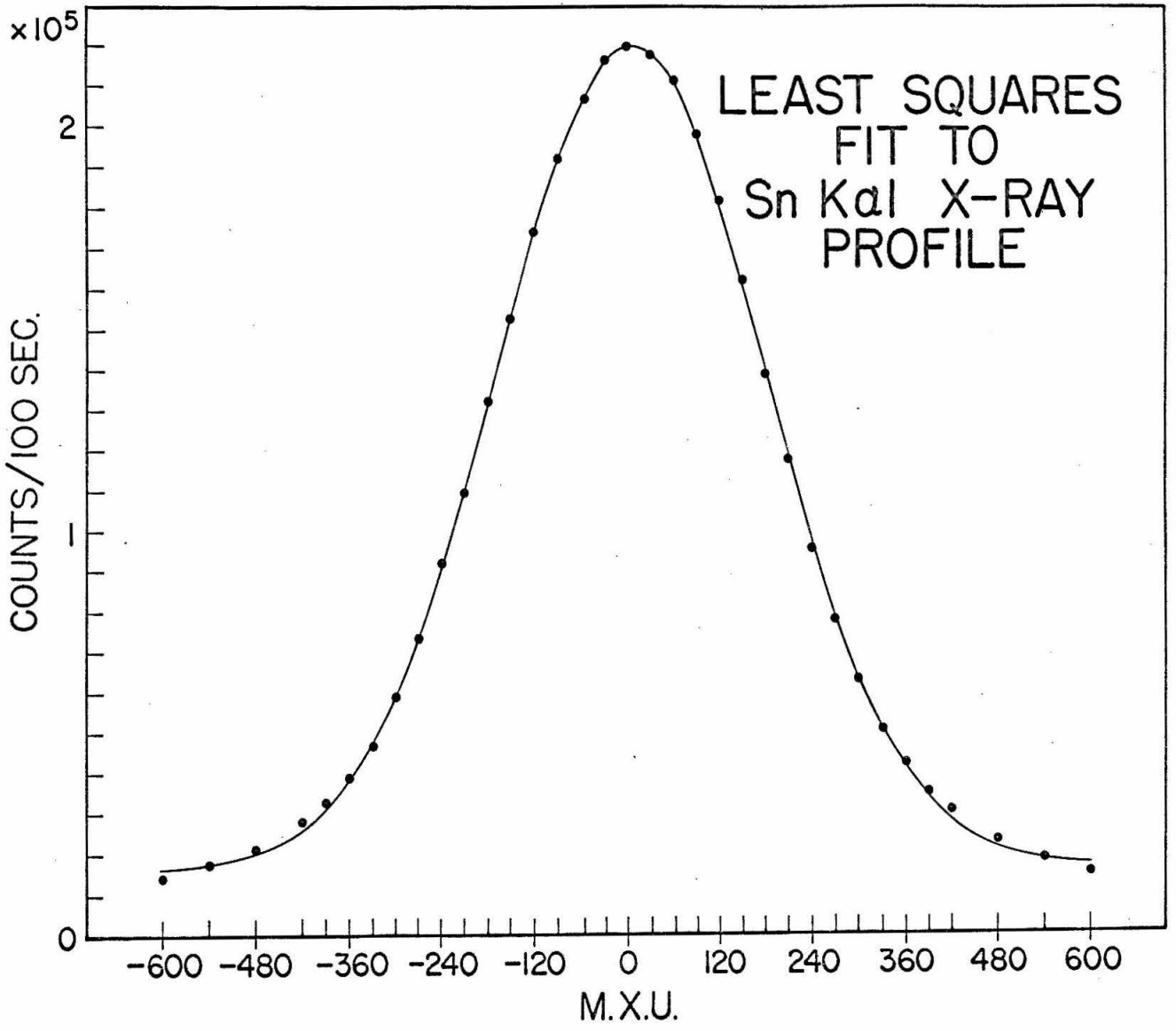
LEAST SQUARES
FIT TO
Sn Kα1 X-RAY
PROFILE
x10^5
2
1
0
COUNTS/100 SEC.
-600 -480 -360 -240 -120 0 120 240 360 480 600
M.X.U.

In the above formula σ is the standard deviation of the mean, N the number of data blocs, $\bar{x}$ the mean value for the shifts, and x_i the shift values corresponding to the individual data blocs. Small corrections must be made to the mean value to obtain the true experimental shift. These corrections concern isotopic impurities of the samples, spectrometer β point corrections, and corrections for elastic scattering and will be discussed in Section V.

Frequency plots of the uncorrected shift values for the individual data blocs are shown in Figure 8. The widths of these distributions reflect the statistical uncertainties in the measurements.

The analysis of the data profiles of the two samples included the quantity X^2 defined below which is a measure of the correspondence between the data and the fitting function. We define

$$X^2 = \frac{1}{N} \sum_{i=1}^{N} \left(\frac{y_i - x_i}{\sigma_i} \right)^2$$

where N = 35 for the number of data points, y_i represents the values of the data to be fit, x_i is the fitting function evaluated at the point i and σ_i are the uncertainties in the data values. All five parameters of the fit plus X^2 for each sample were listed and averaged and the standard deviations about their means were calculated. Differences and ratios of the quantities for the two samples were also calculated by the same computer program. Point plots were made by computer of these quantities for each of the two samples thus showing the variations from one data bloc to another and between one sample and the other. These plots were quite useful in detecting malfunctions of the system,

Figure 8. Frequency plot of uncorrected shifts. The data segment for the plot is the standard data unit bloc and the shifts are plotted at the nearest integral tenth of an M.X.U.

Figure 8

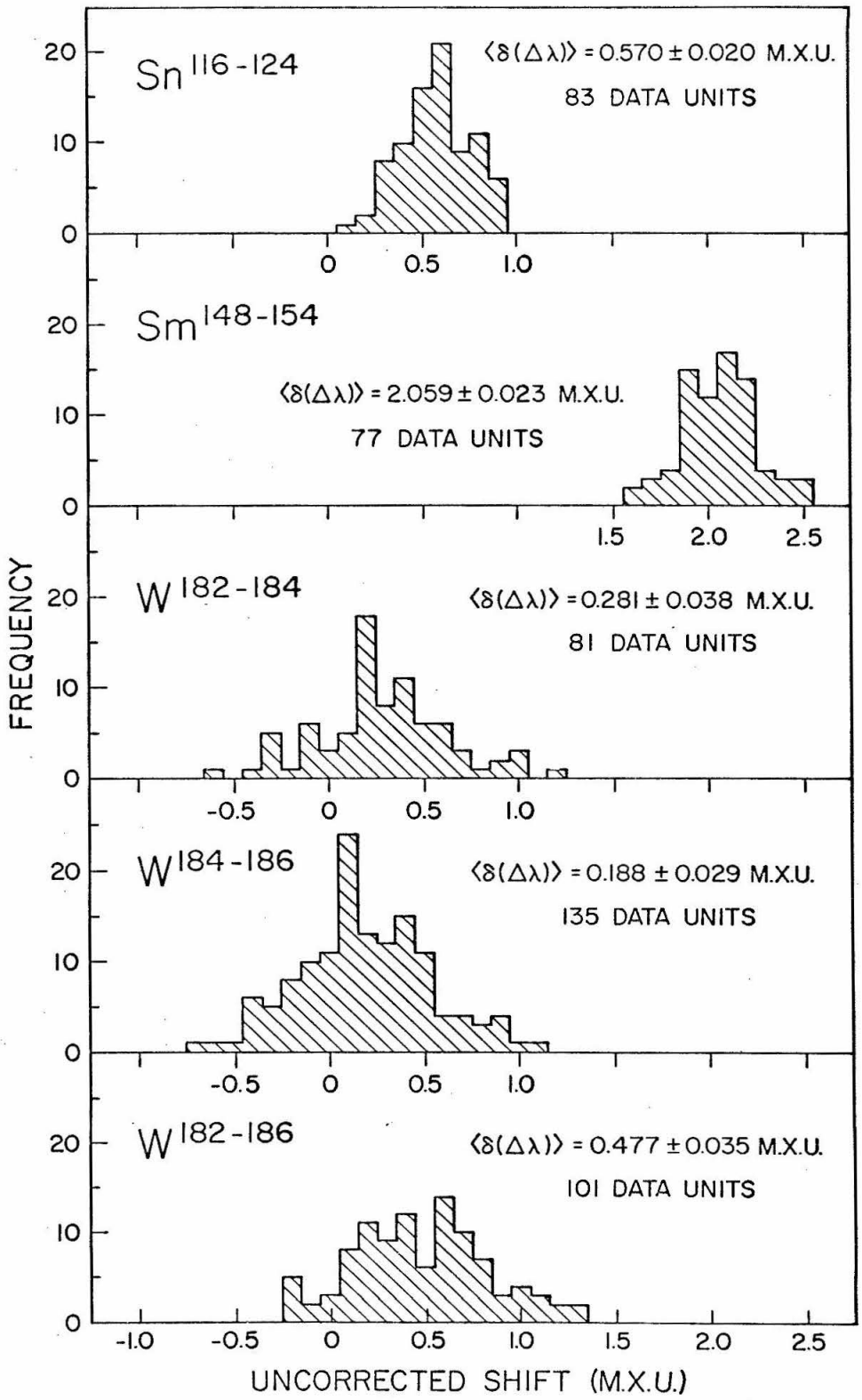
Sn 116-124
⟨δ(Δλ)⟩ = 0.570 ± 0.020 M.X.U.
83 DATA UNITS
Sm 148-154
⟨δ(Δλ)⟩ = 2.059 ± 0.023 M.X.U.
77 DATA UNITS
W 182-184
⟨δ(Δλ)⟩ = 0.281 ± 0.038 M.X.U.
81 DATA UNITS
W 184-186
⟨δ(Δλ)⟩ = 0.188 ± 0.029 M.X.U.
135 DATA UNITS
W 182-186
⟨δ(Δλ)⟩ = 0.477 ± 0.035 M.X.U.
101 DATA UNITS
FREQUENCY
UNCORRECTED SHIFT (M.X.U.)

especially since many types of malfunctions have virtually no detectable effect on the shift result itself, but do show up in one or more of the other quantities analyzed. For example a spectrometer step of irregular size would have little effect on the shift result since both profiles would be rather similarly affected. The malfunction would produce noticeably unusual values for the profile width and peak center parameters however.

C. Systematic Errors

While a Gaussian function has been used to fit the line profiles, a glance at Figure 7 will show that the actual line profiles differed to a small but visible extent from a Gaussian shape. The largest deviations occurred at the extremities of the profile where the characteristic Lorentzian tails are apparent. Because of this small shape mismatch, the half-width and average background parameters of the least square fits were not truly representative of the data. These experiments involved only a comparison, however, and the important point is that the profiles from the two samples had the same shape to a very high degree. The precautions taken in defining the position of the target and in minimizing intensity variations insured that shape differences were indeed small. The residual shape differences may be identified with what we have previously termed aberrational shifts. The magnitude of these shifts is discussed in Section V. The profiles were expected to be slightly asymmetric due to random defects in the diffracting crystal. But such shape irregularities were common to the profiles of both samples, and the fit value for the peak center parameter

defined a center for the slightly irregular line profile. Since the measured shift value involved the difference between two such peak center parameters, any small systematic shape assymetry which may have been present did not cause error in the shift measurements.

In addition to the systematic differences in shape between data profile and fitting function there were also random shape differences caused primarily by random variations in x-ray output over the duration of the four scans comprising the data for a given least square fit. The relatively frequent interchange of samples insured that such random variations were reflected nearly equally in the profiles of both samples. Very small residual differences between the shapes of the profiles of the two samples were of a random nature and were reflected by a slightly larger standard deviation of the measurements about their mean without modifying the value of the mean itself. In order to examine contributions to systematic error due to the data fitting procedure itself, let us consider the effect of small shape differences on the peak center value obtained through a least square fit. By writing down and minimizing the expression for X^2 it may be easily shown for the case of a continuous data function that the peak center parameter resulting from a least squares fit of a single Gaussian function to the sum of several Gaussian functions with relative displacements small compared to their widths is simply the average of the centers of the individual components weighted by their respective areas. Corrections to this desired result are of higher order in the ratio of the small displacement to the profile width. Using the value

10 M.X.U. for a typical aberrational shift from Section III, the higher order correction amounts to a relative error on the order of 10^{-9} in the shift values. Since an uncertainty of the order 10^{-2} in the shift values is present from other sources, as discussed in Section V, systematic errors introduced by the method of data reduction itself may be neglected.

V. EXPERIMENTAL RESULTS AND ERROR ANALYSIS

A. The Uncorrected Shifts

It is convenient to express the directly observed shifts in units of a screw division. One screw division corresponds to one half revolution of the sine screw of the spectrometer. The present spectrometer was designed so that for diffraction by the 310 planes of quartz (as in the present experiments) the screw division scale corresponds to the M.X.U. (10^{-14}cm.) wavelength scale. In the case of the tin I.S. experiment however, allowance for the spectrometer β point must be made to convert screw division units to M.X.U. as discussed in Subsection B. Column 2 of Table 5 shows the directly observed shifts in screw division units. The uncertainties in Column 2 represent the effects of both counting statistics and random drift in the experimental apparatus. The shift sign convention is such that a positive number indicates a harder x ray for the lighter isotope of the pair. This sign convention will be applied to shifts expressed in terms of both wavelength and energy.

Several modifications of the directly observed values of Column 2 must be made to obtain the true I.S. These corrections and allowances for systematic errors are discussed in the subsections to follow.

B. Spectrometer β Point Corrections

If the position of the receiving slit and the orientation of the curved crystal on the spectrometer pivot mount are such that the zero of the screw division scale (pivot arm perpendicular to sine screw)

TABLE 5

1	2	3	4	5	6	7	8	9
Isotope Pair	Uncorrected Shift* (Screw Divisions)	Correction Factors				Measured I.S.		Column 8 Corrected for Mass Shift (mv.)
		Spectrometer β Point	Elastic Scattering	Isotopic Composition	Internal Consistency	(M.X.U.)	(mv.)	
Sn 116-124	0.570 ± 0.020	0.982	1	1.040	1	0.582 ± 0.023	30.0 ± 1.2	35.2 ± 1.3
Sm 148-154	2.059 ± 0.023	1	1	1.017	1	2.094 ± 0.025	272.2 ± 3.3	276.1 ± 3.5
W 182-184	0.281 ± 0.038	1	1.058 ± 0.02	1.067	1.009	0.320 ± 0.037	91.0 ± 10.5	92.3 ± 10.5
W 184-186	0.188 ± 0.029	1	1.058 ± 0.02	1.024	1.010	0.206 ± 0.028	58.6 ± 8.0	59.9 ± 8.0
W 182-186	0.477 ± 0.035	1	1.058 ± 0.02	1.048	0.994	0.526 ± 0.035	149.6 ± 10.0	152.2 ± 10.0

*I.S. sign convention is + when the harder x ray belongs to the lighter isotope.

does not correspond to the zero of the true wavelength scale, then not only will wavelength values read on the screw division scale be in error, but also the dispersion in the M.X.U. scale will be different from that in the screw division scale. From the Bragg formula $n\lambda = 2d \sin\theta$ one obtains the dispersion formula $n\partial\lambda = 2d \cos\theta\,(\partial\theta)$. Thus the dispersion is proportional to the cosine of the diffracting angle θ. A shift measured in screw divisions is transformed to an X.U. shift by multiplication by the factor $\cos\theta_1/\cos\theta_2$ where θ_1 is the Bragg angle for the wavelength in question and θ_2 is the angle indicated by the position of the spectrometer sine screw.

For the cases of wolfram and samarium the spectrometer β point was within 1 X.U. of the zero of the screw division scale and the β point correction could be neglected. For the case of tin however, the curved crystal was intentionally rotated from its normal alignment so that the Kα1 line at 489.57 X.U. could be accommodated. This change was necessary since the spectrometer sine screw had sufficient travel to accommodate wavelengths only up to 400 X.U. The β point correction factor for the tin experiment amounted to 0.982 as shown in Column 3 of Table 5.

C. Elastic Scattering Corrections

A small percentage of the x rays passing through the receiving slit originate not from the fluorescence of the sample material, but from x rays scattered elastically by the sample material. These are x rays originating from the external tube whose wavelength is just equal to the Kα1 wavelength of the sample material. Therefore they satisfy the conditions for Bragg diffraction in the spectrometer. If

the wavelength distribution of the radiation from the wolfram anode of the external tube is sufficiently like a straight line over the region of the Kα1 x-ray scan, as it is in the cases of tin and samarium, this small amount of elastic scattering merely contributes to the background. In the case of the wolfram measurements however, the external radiation of course has a resonance peak at the wolfram Kα1 energy.

Thus, in the case of wolfram the elastic scattering process will add a contribution to the peak as well as to the background. This elastic scattering piece is independent of the isotopic composition of the sample and will therefore decrease the shift observed between the two samples. As a first step in estimating the correction to be applied for the elastic scattering in the wolfram measurements, a sample of tantalum (Z = 73) foil of optimum thickness was placed in the spectrometer and a scan of the wolfram (Z = 74) Kα1 region was carried out. The peak to background ratio in the resulting profile was found to be 2.1. With a wolfram sample in the spectrometer a scan of the same region yielded a peak to background ratio of approximately 40. The elastic scattering contribution to the wolfram Kα1 peak with the wolfram sample was then assessed to be 2.1 expressed in units of the common background level. Thus the peak to background ratio for the fluorescent component with the wolfram sample is given by $40-2.1 \approx 38$, and the ratio of elastically scattered x rays to fluorescent x rays with the wolfram sample is equal to 2.1/38 = 0.055. The observed shifts in the wolfram experiments must therefore be multiplied by the factor 1/0.945 to obtain the true shifts between the samples. Including an estimate of the error involved in the above procedure we obtain a correction factor of 1.058 ±

.02 as indicated in Column 4 of Table 5.

D. Isotopic Composition Corrections

The samples used in these experiments were enriched isotopically. The actual isotopic compositions of the samples used are given in Table 4. This information was supplied by ORNL who carried out the mass separations. Since the samples used were not quite isotopically pure, a small correction must be applied to the observed shifts. In order to make such a correction exact it would be necessary to know the actual I.S. among the various isotopes. However, since the corrections to be made are relatively small it is sufficient to have approximate information on the relative shifts, which in this case will be obtained from optical I.S. data.

The calculational procedure used in making the isotopic composition correction is described below. The relative optical shift data used in the corrections are presented in Table 6. The wavelengths of the Kα1 x rays are given by $\lambda_{Z,A} = c_Z + \Delta\lambda_{Z,A}$ where $\Delta\lambda_{Z,A}$ are the values given in Table 6 and c_Z is a constant for a given value of Z which has been suppressed. The units are arbitrary. The degree of precision of the relative optical shift data necessary in order to make errors from this source negligible is only on the order of 20-30%, which is a much larger error than would be expected from these data. In the formulae below we deal with a vector space of dimensionality equal to the number of stable isotopes of the element considered. X is the observed I.S. and $\vec{S}^A$ and $\vec{S}^B$ are the isotopic compositions of the two samples being compared normalized so that the scalar sum of the com-

TABLE 6

Relative Optical I.S. Data Used in Correcting for the Isotopic Composition of the Targets. The values in parentheses have been obtained by interpolation.

Isotope	Relative Wavelength
W	
180	0[32])
182	0.68
183	(1.18)
184	1.68
186	2.56
Sm	
144	0[32])
147	(1)
148	2
149	(2.57)
150	3.14
152	4.81
154	5.72
Sn	
112	0[33])
114	6.7
115	(9.8)
116	12.9
117	(15.25)
118	17.6
119	(19.8)
120	22.0
122	23.5
124	25.0

ponents is equal to one. The vector $\vec{\lambda}$ represents the true wavelengths of the Kα1 x rays for the various isotopes. The vector $\vec{A}$ defined below contains the relative I.S. information obtained from the optical data. The scalar b and vector $\vec{c}$ defined below which relate the relative isotope wavelengths to the absolute wavelengths can be considered unknowns since they do not appear in the final results for the isotopic composition correction given in Equation (V.3). The vector $\vec{c}$ is defined to have equal components along each axis of the vector space. We define $\vec{D} = \vec{S}^A - \vec{S}^B$. Then we have

$$\vec{\lambda} \cdot \vec{D} = X \quad . \tag{V.1}$$

Introducing the relative I.S. information $(\vec{A})$ we set

$$\vec{\lambda} = b\vec{A} + \vec{c} \quad . \tag{V.2}$$

Eliminating $\vec{\lambda}$ from (V.1) we have $b\vec{A} \cdot \vec{D} + \vec{c} \cdot \vec{D} = X$. Solving for b, we have

$$b = \frac{X - \vec{c} \cdot \vec{D}}{\vec{A} \cdot \vec{D}} \quad .$$

Substitution in (V.2) gives

$$\vec{\lambda} = \frac{(X - \vec{c} \cdot \vec{D})}{\vec{A} \cdot \vec{D}} \vec{A} + \vec{c} \quad .$$

We then have

$$\text{true I.S.} = \lambda_1 - \lambda_2 = \frac{(X - \vec{c} \cdot \vec{D})(A_1 - A_2)}{\vec{A} \cdot \vec{D}} \quad .$$

From the definitions of the vectors $\vec{c}$ and $\vec{D}$ it follows that $\vec{c} \cdot \vec{D} = 0$.

Therefore,

$$\text{true I.S.} = \frac{X(A_1 - A_2)}{\vec{A} \cdot \vec{D}} \quad .$$

The correction factor to be applied to the observed wolfram shifts is therefore given by

$$\text{correction factor} = \frac{A_1 - A_2}{\vec{A} \cdot \vec{D}} \qquad (V.3)$$

The numerical correction factors are given in Column 5 of Table 5.

E. Internal Consistency Constraint

In the case of wolfram three shifts were measured in the present experiments: W182-184, W184-186, and W182-186. The values of Column 2 of Table 5 corrected by the factors of Columns 3 to 5 are independent measurements. The precision of these measurements may be improved by applying the constraint

$$\text{I.S.}(182\text{-}184)_f = C\left[\frac{\text{I.S.}(182\text{-}184)_o}{\Delta^2(182\text{-}184)} + \frac{\text{I.S.}(182\text{-}186)_o - \text{I.S.}(184\text{-}186)_o}{\Delta^2(182\text{-}186)+\Delta^2(184\text{-}186)}\right]$$

with similar equations for the other two cases. The subscript "o" indicates the values of Column 2 corrected by the factors of Columns 3 to 5 and "f" indicates the final value. The Δ's are the uncertainties in the I.S. and C is a normalization factor given by

$$C = \left[\frac{1}{\Delta^2\,(182\text{-}184)} + \frac{1}{\Delta^2(182\text{-}186)+\Delta^2(184\text{-}186)}\right]^{-1} .$$

Analagous formulae apply to the other two measured wolfram shifts. The uncertainties in the I.S. values are reduced approximately by the factor $\sqrt{2/3} \approx 0.82$ by application of the constraint illustrated above.

The correction factors resulting from this internal consistency constraint are given in Column 6 of Table 5.

F. Aberrational Errors

Ideally the center of the profile produced by the Cauchois spectrometer is invariant with respect to small displacements of the source. In practice however, profile shifts on the order of 10 M.X.U. may be produced by placing a relatively small source in various positions with respect to the crystal. Such shifts may be called aberrations and result from the vertical divergence effect and from imperfections in the crystal structure and bending. Aberrational shifts may be produced not only by varying the position of a small sample but also by varying the intensity distribution across the surface of an extended sample like the ones used in the present experiments. The observed profile may then be considered to be a weighted sum of the constituent profiles from different parts of the crystal, the weights being in proportion to the luminosity of that part of the sample associated with the particular area of the crystal.

Direct measurement of aberrational shifts using two sample holders similar to those used in the measurements, but containing natural H_2WO_4 at optimum thickness yielded a shift of $0.00 \pm .04$ M.X.U.

A second experimental method was employed to better estimate the magnitude of the aberrational shifts to be expected in these experiments. In this method two wolfram samples were prepared. These samples were similar to those used in the actual measurements except that both samples were of natural isotopic composition, and both were

of only half the optimum thickness. Because the aberrational shifts depend on the variations in intensity across the surface of the extended samples, they will be exaggerated by the samples of half-optimum thickness. Intensity variations are much greater for a given variation in actual thickness for these samples. The samples used in the actual I.S. experiments were prepared with sufficient care to insure that they came within 5% of the optimum mass thickness. Assuming the maximum 5% error in mass thickness we estimate from Figure 4 a slope of 700 cm^2/g-sec. at the operating point 5% less than the optimum thickness of 0.1753 g/cm^2. With the linear extrapolation from the figure at 0.14 g/cm^2 thickness down to 0 we can approximate the slope at half optimum thickness to be about 4550 cm^2/g - sec. Thus the half optimum thickness targets can be expected to multiply aberrational shifts by the factor 4550/700 = 6.5 when compared to those of optimum thickness used in the actual experiments. The shift measured between the wolfram samples of half optimum thickness was 0.04 ± 0.05 M.X.U. The deviation of this value from 0 represents the effect of aberrational shifts. Applying the adjustment factor 1/6.5 we then estimate the aberrational error in the actual I.S. experiments to be on the order of 0.006 M.X.U.

With this estimate of the aberrational error as a guide a value 0.01 M.X.U. has been adopted as the uncertainty due to this source. The final values of the I.S. with uncertainties including this contribution from the aberrational error are given in Columns 7 and 8 of Table 5 in wavelength and energy units.

G. Chemical Shift Errors

Systematic error due to chemical shifts in the Kα1 x-ray energies must also be considered if the two samples are of different chemical composition. Such chemical shifts between the oxides of tin and the metal itself have been measured by Sumbaev and Mezentsev [34], and Gokhale et al. [35] in this laboratory using a technique similar to that employed in the present measurements. The chemical shifts observed by these investigators between SnO and SnO_2 is about 80 mv., which is several times larger than the measured Sn 116-124 I.S. One would also expect to find x-ray shifts between different crystalline forms of a single compound. These shifts have not yet been observed, but they would be expected to be somewhat smaller than the shifts between compounds of differing oxidation state such as SnO and SnO_2. The chemical compounds used in the present experiments were SnO_2, WO_3, and Sm_2O_3, prepared by ORNL by standardized procedures so that all isotopic samples of a given element received the same chemical processing. In order to verify that the isotopic samples were of identical chemical structure, high resolution powder pictures were obtained of each sample using a Guinier camera. With this method it was possible to distinguish between and identify not only compounds of different oxidation states but also different crystalline structures of a given compound.

In the case of the WO_3 samples, an upper limit of 1% was placed on the presence of forms other than the unique monoclinic structure described in the literature [36] for WO_3 at room temperature .

For the upper limit of the systematic error to be expected in the wolfram measurements we may then take 100 mv., a typical chemical shift value, which at the upper limit of 1% impurity would constitute a shift of 1 mv. This uncertainty may be neglected in comparison to those from sources previously discussed. Longer Guinier camera exposure in the case of the SnO_2 samples established an upper limit of 0.25% on the presence of impurities along with the expected tetragonal structure. We thus estimate the systematic error contribution in this case to be about 0.25 mv. which again will be neglected in comparison to the larger uncertainties from other sources.

In the case of Sm_2O_3, four crystalline structures are indicated in the literature to be possible at room temperature. In the samarium samples as received from ORNL three of the structures were found to be present in the Sm148 sample while the Sm154 sample contained a mixture of all four structures. By heating the samples in air at 1300° C for twenty-four hours the samples were reduced to a single B-type structure in agreement with the observations of Curtis and Johnson [37]. In this case an upper limit of 0.5% is estimated on the level of impurity structures after the roasting process. This yields 0.5 mv. as an upper limit of error which again may be neglected. A comparison of I.S. measurements in the samarium case before and after reduction to a unique crystalline form may be used to give semiquantitative estimates of the Kα1 shift caused by differences in crystal structure. It is difficult to estimate accurately the relative amounts of the four crystalline structures present in the samarium

samples before the roasting treatment. However, the difference in the shift measurements before and after roasting of (-6.4 ± 4.6) mv and an estimate of 10% difference in crystal mixture population indicates that shifts among samples of Sm_2O_3 of different crystal structures of the order of magnitude of 50 mv might be expected.

Guinier exposures of the Sm_2O_3 samples after completion of the I.S. measurement showed no structural changes due to exposure of the material to the x-ray radiation.

H. Final Observed Shifts

The final observed I.S. values are given in Columns 7 and 8 of Table 5 in wavelength and energy units. The uncertainty represents one standard deviation. In Column 9 are the I.S. values of Column 8 corrected by subtracting the normal and specific mass shifts. In the next section the information on the change in the nuclear charge radii will be extracted from the data according to the discussion of Section II.

VI. NUCLEAR SIZE RESULTS

In this section are the results for the changes in rms nuclear charge radii as determined by the measured I.S. and the calculated nuclear-atomic coupling described in Section II. The calculations of Section II have been estimated to contribute an over-all uncertainty of 2% to the results. This uncertainty is included in the error estimates given below. Discussion of the results will be reserved to the next section.

Column 2 of Table 7 contains the theoretical I.S. values $\delta(\Delta E)_B$ calculated by Babushkin [12]. Babushkin's results have taken into account the electrostatic volume effect, including the screening effect on the electron making the transition of the other electrons in the atom. Column 3 of Table 7 is a revision of the results of Column 2 made by including the effects of the screening by the electron involved in the transition on the other atomic electrons, nuclear polarization, and the radiative correction to the electron magnetic moment interaction. The entries of Column 3, $\delta(\Delta E)_{std}$, are the predicted I.S. assuming a rms nuclear radial dependence of $1.2 \times 10^{-13} A^{1/3}$ cm. It should be noted that in order to include the small effects of nuclear polarization in the values of Column 3, information on the deformations of the nuclei was necessary. For this purpose the deformations given by Babushkin [13] were employed. The nuclear polarization effect contributes about 4% to the I.S. in the case of Sm 148-154 and is negligible in the cases of Sn and W here considered.

TABLE 7

Nuclear Size Results

1	2	3	4	5
Isotope Pair	$\delta(\Delta E)$	$\delta(\Delta E)_{std}$ (mv)	$\delta(\Delta E)_{exp}$ (mv)	$\delta(\Delta E)_{exp}/\delta(\Delta E)_{std}$
Sn 116-124	76.9	69.7	35.1 1.3	0.504 0.025
Sm 148-154	177.0	158.4	276.1 3.5	1.743 0.042
W 182-184	152	141.7	92.3 10.5	0.651 0.079
W 184-186	151	138.9	59.9 8.0	0.431 0.061
W 182-186	303	280.6	152.2 10.0	0.542 0.038

In Column 4 of Table 7 the mass shift corrected I.S., $\delta(\Delta E)_{exp}$ are repeated for comparison to the theoretical values of Column 3. Column 5 contains the ratio $\delta(\Delta E)_{exp}/\delta(\Delta E)_{std}$ formed from the values of Columns 3 and 4. This ratio represents the actual change in rms nuclear charge radius expressed in units of $\delta R = 1.2 \times 10^{-13}$ $\delta(A^{1/3})$ cm. The heavier isotope was the larger in all of the cases met with in the present experiments. The uncertainties expressed are due to both the measurements and the coupling calculations and should therefore provide an indication of the over-all precision of the results.

VII. DISCUSSION OF RESULTS

A. Direct Experimental Comparisons

It is the aim of this subsection to make such direct experimental comparisons as are possible in order to test the general agreement of the present results with independent measurements. These comparisons will be relatively free of error due to theoretical calculation but will be limited in number as a result.

There are no other atomic x-ray measurements among the Sn or W isotopes. For the case of Sm, however, we have the measurements of Sumbaev and Mezentsev [7] which give the shifts

Sm 144-150 $\quad \delta(\Delta E) = 245 \pm 20$ mv

and Sm 144-152 $\quad \delta(\Delta E) = 340 \pm 20$ mv .

Since the present experiment with Sm involved the isotopes 148 and 154, direct comparison is not possible. We may make use of the fairly high precision of the relative optical electron shift measurements which have been carried out for all the above isotopes of Sm to make a comparison more indirect, but still not too dependent upon theoretical assumptions or calculations. Using the value (272.2 ± 3.3) mv of the Sm 148-154 shift measured in the present work, and the results for the relative optical shifts

Sm	144	148	150	152	154
relative energy (arbitrary units)	0	2	3.14	4.81	5.72

given by Brix and Kopfermann [32], we can derive the values expected for the shifts measured by Sumbaev and Mezentsev given above. Assuming a

negligible uncertainty in the relative optical results we obtain the shifts

Sm 144-150 $\delta(\Delta E) = 230 \pm 3$ mv

and Sm 144-152 $\delta(\Delta E) = 352 \pm 4$ mv .

The results derived from the present experiment show good agreement with the measurements of Sumbaev and Mezentsev.

B. Indirect Experimental Comparisons

Here we shall compare the results of the present experiments to similar measurements involving the optical shift and muonic x-ray shift techniques. The nature of the agreement in such comparisons depends on the accuracy of the theoretical calculations of the I.S. in each of the cases as well as the accuracy of the measurements involved.

In Table 8 the nuclear size results of the three methods are compared. The muonic x-ray data [38] * have been extrapolated by using relative shift information from optical measurements in the case of the Sn 116-124 entry. The optical results are from a compilation by Babushkin [13]. It should be noted that the theoretical values $\delta(\Delta E)_{std}$ for the optical I.S. have included only the volume effect and screening by the non-transition electrons. The comparisons of Table 8 are illustrated in Figure 9 which shows the agreement to be good except for the ratio of the shifts in W182-184 and W184-186. The optical shift measurements [32] give the result 0.88 for this ratio. The uncertainty in this value ought not to be more than a few percent.

*The muonic x-ray values presented here are averages of the $K\alpha 1$ and $K\alpha 2$ shift results.

TABLE 8

Comparison of X-Ray, Optical, and Muonic I.S.

Isotope Pair	$\delta(\Delta E)_{exp}/\ \delta(\Delta E)_{std}$		
	Present X-Ray Work	Optical	μ X Ray
Sn 116-124	0.504 ± 0.025	0.33 ± 0.15	(0.41 ± 0.04)
Sm 148-154	1.743 ± 0.042	1.67 ± 0.35	
W 182-184	0.651 ± 0.079	0.45 ± 0.08	0.65 ± 0.10
W 184-186	0.431 ± 0.061	0.40 ± 0.07	0.55 ± 0.10
W 182-186	0.542 ± 0.038	0.42 ± 0.07	0.60 ± 0.07

Figure 9. Comparison of x-ray, optical, and muonic I.S. The data are from Table 8.

Figure 9

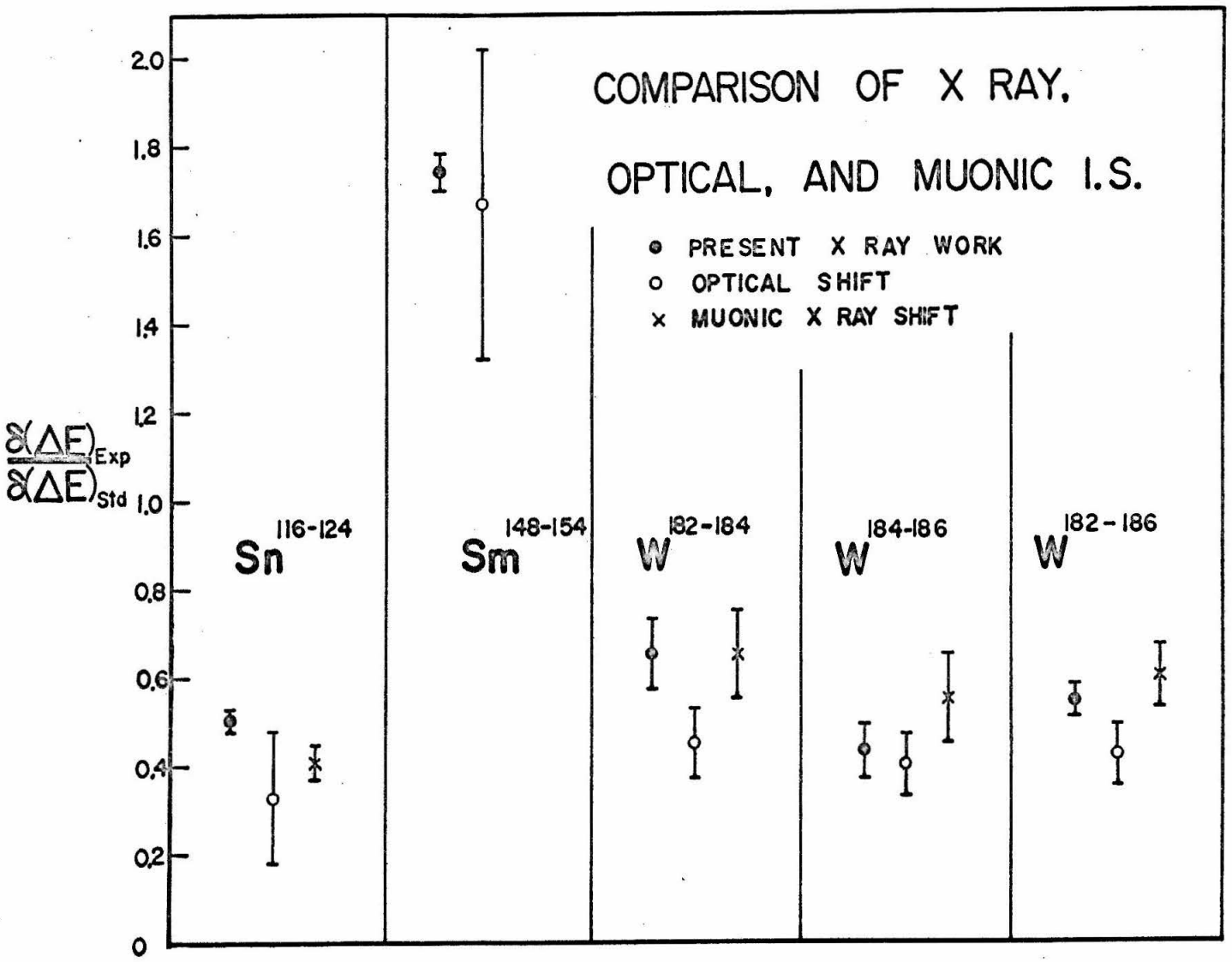
COMPARISON OF X RAY,
OPTICAL, AND MUONIC I.S.
PRESENT X RAY WORK
OPTICAL SHIFT
MUONIC X RAY SHIFT
δ(ΔE)Exp / δ(ΔE)Std
2.0
1.8
1.6
1.4
1.2
1.0
0.8
0.6
0.4
0.2
0
Sn 116-124
Sm 148-154
W 182-184
W 184-186
W 182-186

The present measurements yield a value 0.64 ± 0.12 for this ratio. A third value 0.78 ± 0.28 may be obtained from the μ shift experiments[38] but the uncertainty here is too large to provide much help in settling the discrepancy between the optical and x-ray results. Although specific mass corrections for the optical I.S. are not known, (the optical data has been corrected only for the normal mass shift) it seems highly unlikely that they could be of sufficient importance to produce the observed discrepancy. Additional measurements would seem to be desirable.

C. The Brix-Kopfermann Diagram

Figure 10 is a Brix-Kopfermann diagram [32] summarizing the I.S. data for the cases of Sn, Sm, and W. The optical shift results are subject to an uncertainty on the order of 20% because of the large screening correction to the penetration of the optical electrons into the nucleus. This screening uncertainty does not apply to the relative size of the shifts from one isotope pair to another of the same element. The uncertainty in the relative optical shift is largely experimental in nature and should be about 5% or smaller. In the case of the x-ray I.S. the screening corrections to the electron penetration are smaller and more easily estimated. In this case absolute accuracy is limited primarily by the experimental uncertainty which may be minimized by measuring the x-ray shifts between isotopes of the maximum neutron separation possible. The x-ray and optical data may then be considered complementary in nature, the optical data providing the relative shifts and the x-ray data providing the absolute calibration

Figure 10. Brix-Kopfermann diagram comparison of present results with optical and muonic x-ray I.S. The points represent two-neutron shifts and are plotted against the neutron number of the heavier isotope.

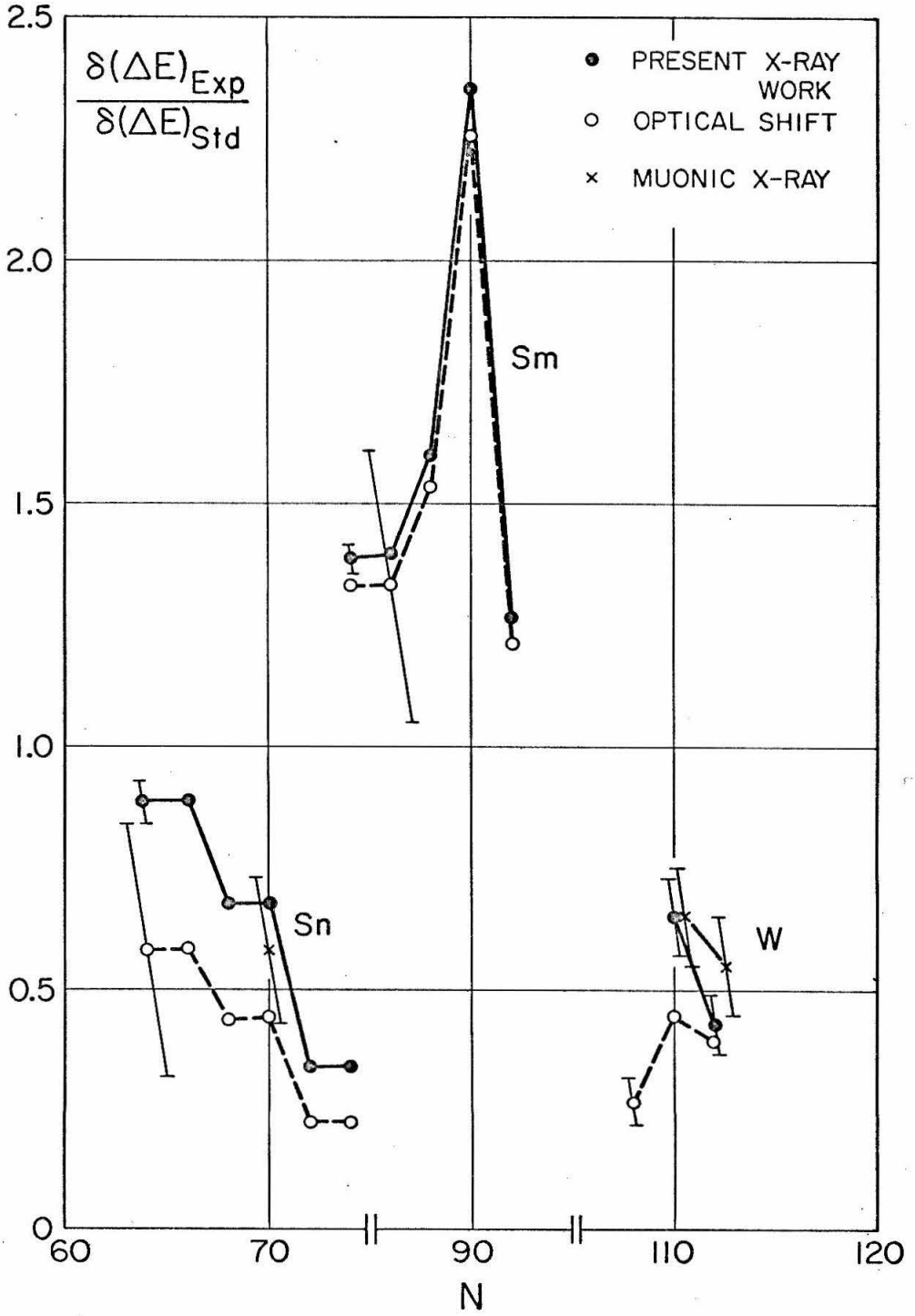
2.5
2.0
1.5
1.0
0.5
0
δ(ΔE)Exp / δ(ΔE)Std
PRESENT X-RAY WORK
OPTICAL SHIFT
MUONIC X-RAY
Sm
Sn
W
60
70
90
110
120
N

Figure 10

of the shifts. For lighter elements such as Sn (Z = 50) the complementarity is not so complete since the unknown specific mass corrections in the case of the optical measurements make even the relative shifts subject to an uncertainty above the small experimental one. Even in such cases however, the synthesis of the x-ray and optical shift data along the lines described above would appear to be the best method of analysis at the present time. More numerous and more precise x-ray shift measurements could well eliminate the need for reliance on the optical data for the relative shifts. In the case of wolfram, the present results are presented independently of the optical data since they involved two-neutron shifts.

In Figure 10 the optical data are connected by a dashed line for each element. A single bar represents the absolute uncertainty for the group. Since the relative uncertainties are smaller, the uncertainty makes it possible to shift the groups as a whole up or down on the diagram. The results of the present x-ray shift measurements are presented as points connected by a solid line. Again a single error bar represents the absolute uncertainty for the group after "normalization" of the optical results by the x-ray results in the cases of Sn and Sm.

D. Macroscopic Nuclear Models

In the so-called macroscopic approach to the analysis of I.S. phenomena, nuclear properties are supposed to vary gradually and smoothly from one nuclide to another, without the abrupt discontinuities characteristic of a shell model. The earliest and most simple

macroscopic approaches to the prediction of the I.S. assumed the rms charge radius to vary as $cA^{1/3}$, with the numerical coefficient "c" being taken from the current electron scattering results. This constant density model gave rise to the first of the "I.S. anomalies" because the observed shifts are on the average only about one half of the value predicted by this model. This "anomaly" is clearly illustrated by the well-known Brix-Kopfermann diagram (Figure 11) showing the optical shift data given by Babushkin [13].

The $A^{1/3}$ model has been refined by adopting the more accurate formula for the average equivalent nuclear charge radius given by Elton [39]. He found the best fit to electron scattering data to be

$$R = 1.121\ A^{1/3} + 2.426\ A^{-1/3} - 6.614\ A^{-1}\ .$$

The adoption of this radial dependence on A leads to the prediction of a somewhat smaller I.S. than does the $A^{1/3}$ model, the reduction factor assuming values of 0.90 to 0.833 from $_{82}Pb$ to $_{37}Rb$, respectively [12]. This small reduction in the predicted shifts is four or five times too small to account for the I.S. "anomaly."

The crude $A^{1/3}$ model and its refinement by the Elton formula suffer from the assumption that the variation of the nuclear charge radius along the "mass stability valley," well described by the $A^{1/3}$ law or its refinements, is identical to the variation of the nuclear charge radius along the direction of neutron addition. This assumption may be abandoned by allowing the charge radius to vary differently along the "mass stability valley" and along the lines of constant Z. The difference in charge radius variation along the two directions

Figure 11. Brix-Kopfermann diagram of optical I.S. The points represent two-neutron shifts and are plotted against the neutron number of the heavier isotope. Different symbols are used only to improve clarity.

Figure 11

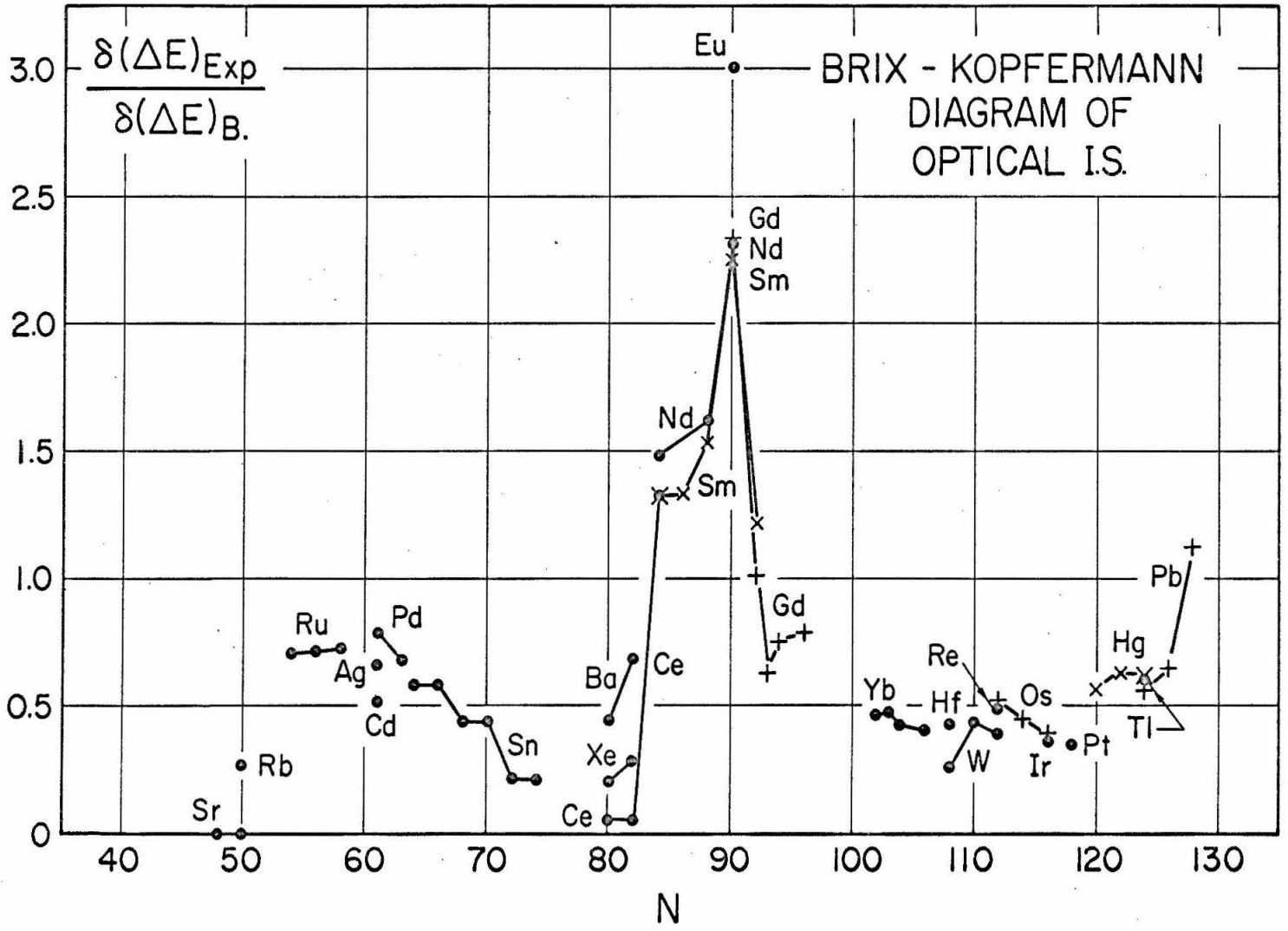
BRIX - KOPFERMANN
DIAGRAM OF
OPTICAL I.S.
δ(ΔE)Exp / δ(ΔE)B.
3.0
2.5
2.0
1.5
1.0
0.5
0
40
50
60
70
80
90
100
110
120
130
N
Eu
Gd
Nd
Sm
Nd
Sm
Gd
Pb
Ru
Pd
Ag
Cd
Sn
Rb
Sr
Ba
Ce
Xe
Ce
Re
Hg
Yb
Hf
Os
Tl
W
Ir
Pt

of the Z-N plane is ascribed to the interplay between the nuclear Coulomb energy and the bulk compressibility of nuclear matter. That is, the addition of a proton to a given nucleus may be expected to increase the nuclear charge radius more than the addition of a neutron because in the former case the additional Coulomb repulsion acts to further expand the nucleus if it has finite compressibility. The compressibility analysis as applied to the I.S. is described in detail by several authors [40,41,11].

Aside from the limitations inherent in a "bulk" treatment of nuclear properties, the theory suffers from the unwarranted neglect of interactions which compete with the variation of Coulomb energy with nuclear density to change the nuclear radius. Such terms would include, for example, neutron-proton symmetry energies [11]. For this reason, compressibility coefficients based on I.S. data and calculated including only the Coulomb repulsion effect cannot be expected to contribute much to our knowledge about the compressibility of nuclear matter.

In the case of deformed nuclei, a change in the intrinsic quadrupole deformation between isotopes also contributes to the I.S. as discussed in Section II. Fradkin [17] has introduced the concept of "quadrupole deformation compressibility" in analogy with what might be called the "monopole compressibility" mentioned above. The deformation compressibility is a phenomenological approach to provide an additional degree of freedom to accommodate the I.S. data. The numerical value of the deformation compressibility parameter chosen by Fradkin de-

creases the deformation contribution to the I.S. by approximately one half. In this way the classical [40] second isotope shift anomaly concerning variations of the I.S. in the regions of deformed nuclei may be fairly well accounted for.

The third classical anomaly of the even-odd staggering is of course not dealt with in the bulk theory. Irregular variations of the I.S. within the reach of present experimental methods are also ignored in this analysis. Further, the important phenomena of isomer shifts are outside the framework of the bulk theory. Recent isomer shift experiments involving the 0^+ and 2^+ states of Sm 152 have been carried out using Moessbauer technique [42] and also with muonic atoms [43]. These studies show that

$$\frac{\delta R}{R} \approx 5 \times 10^{-4}$$

between these states. The present Sm 148-154 experiment yielded

$$\frac{\delta R}{R} \approx 2 \times 10^{-2}$$

between the two isotopes. For a single-neutron shift in Sm we would then expect, on the average,

$$\frac{\delta R}{R} \approx 3 \times 10^{-3} \quad .$$

The isomeric charge radius change is thus about 1/6 of the single-neutron isotopic change in this case. A precise calculation of nuclear charge radius effects would be required to recognize such level effects. In summary then, the macroscopic nuclear analysis is able to reproduce the average trend of the Brix-Kopfermann diagram well, but lacks the capability to explain local variations and provides only limited impli-

cations concerning nuclear structure because of its phenomenological nature.

In comparing the present mass-shift corrected results with the predictions of the macroscopic model, we have included all the atomic effects as set forth in Section II. The theoretical values of Babushkin [12,13] which include effects of the compressibilities, deformation, and Elton's radius formula are used with modification for the effects of screening by the transition electron, nuclear polarization, and the interaction between the nuclear electric field and the electron magnetic moment. The ratios $\delta(\Delta E)_{exp}/\ \delta(\Delta E)_{bulk}$ are presented in Table 9.

E. Microscopic Nuclear Models

It is clear that a theoretical model must allow for single particle or shell effects if it is to explain the observed fluctuations in the I.S. between neighboring isotope pairs as in the case of Sn (see Figure 11). A calculation based on such a model has been made by Bunatyan and Mikulinskii [44]. These authors apply to the case of the I.S. of near-spherical nuclei the nuclear theory developed by Migdal [45] and Larkin [46] which is based on the Fermi liquid theory of Landau [47]. In this model of a finite Fermi system, two phenomenological quasi-particle interaction constants are introduced in order to best reproduce the I.S. and quadrupole moment data. One constant characterizes the intranuclear interaction in the internal regions of the nucleus and the other constant applies to interactions at the nuclear surface. The general agreement between the I.S. data and these calculations is good

TABLE 9

Isotope Pair	$\delta(\Delta E)_{exp} / \delta(\Delta E)_{bulk}$
Sn 116-124	0.83 ± 0.03
Sm 148-154	1.55 ± 0.02
W 182-184	1.29 ± 0.15
W 184-186	0.73 ± 0.10
W 182-186	0.99 ± 0.07

for $Z > 60$. For $Z < 60$ the calculated shifts are about twice as large as the experimental values. Local I.S. variations are partially reproduced. The trend of experimental quadrupole moments is also attained, but somewhat different interaction constants from those employed in the I.S. case were used to best reproduce the quadrupole moment data. A comparison between the calculated I.S. for the even Sn isotopes, the optical data, and the optical data renormalized by the present work is given in Table 10. The renormalization of the optical data by use of the present results improves the agreement with the calculated values. It should be noted that the optical and present Sn results differ by the factor 0.654 because of both different measurements and different atomic coupling calculations which provide relative factors of 0.722 and 0.906 respectively. Since the values of Bunatyan and Mikulinskii in Table 10 are based on the atomic coupling calculation used for the optical data their values strictly should be increased by 1/.906 in order to make a comparison with the present results.

An I.S. calculation has also been carried out by Uher and Sorenson [48] using the pairing plus quadrupole model. In this treatment the nuclear system is divided into a core plus a few valence particles. Monopole and quadrupole polarizations of the core by the valence particles are treated in a phenomenological manner. The independent particle configuration of the valence particles is admixed by the pairing plus quadrupole interaction and the resulting wave functions are used to calculate the I.S. Only near-spherical nuclei of the even-even and odd-even types are treated. All but one of the

TABLE 10

Isotope Pair	$\delta(\Delta E)_{exp}/\ \delta(\Delta E)_{std}$		$\delta(\Delta E)_{calc}/\delta(\Delta E)_{std}$	
	Optical Data	Present Data	Bunatyan et al Calculation	Uher et al Calculation
Sn 112-114	0.58 ± .15	0.89 ± 0.04	0.94	0.498
Sn 114-116	0.58 ± .15	0.89 ± 0.04	0.94	0.501
Sn 116-118	0.44 ± .15	0.68 ± 0.03	0.95	0.482
Sn 118-120	0.45 ± .15	0.68 ± 0.03	0.97	0.462
Sn 120-122	0.22 ± .15	0.34 ± 0.02	0.43	0.458
Sn 122-124	0.22 ± .15	0.34 ± 0.02	0.43	0.461
Sm 148-150	1.54 ± .36	1.48 ± 0.04	-	1.176
Sm 150-152	2.25 ± .47	2.16 ± 0.05	-	3.481

phenomenological parameters in the model are determined by satisfying average charge radius effects over the periodic table, while the remaining one is selected to give the best agreement with both isotope and isomer shifts. The average trends of the I.S. data are well reproduced by the calculations. There is only partial success in reproducing the abrupt local variations, as in the case of the Sn isotopes. In this model these local variations are caused largely by changes in the quadrupole interaction.

In Table 10 the calculations for Sn and Sm are compared with the results of optical shift and the present measurements. The entries under the present work heading are renormalizations of the optical results using the present x-ray data. In comparing the Sm results, again one must be aware that of the 0.96 ratio of optical to present results, a factor 0.895 arises from the different atomic coupling effects included and a factor 1.07 comes from the measurements themselves. Again the theoretical values of Uher and Sorenson are based on the atomic coupling used for the optical data so that the theoretical values should be increased by the factor 1/0.895 when being compared to the present results in Table 10.

A recent calculation by Perey and Schiffer [49] incorporating an isospin dependent term in the nuclear optical potential has succeeded in reproducing the general trend (radii increasing more slowly than $A^{1/3}$) of the I.S. data. In this calculation the isospin term of the potential was taken to have the same Woods-Saxon shape as the scalar part, and the well depth was chosen to match the last-proton

binding energy. Unfortunately, no numerical predictions are given for the heavier nuclei ($A > 50$) which are involved in the present study. An extension of this calculation to provide such numerical values would appear to be extremely valuable.

In summary, the microscopic calculations so far available are only partially successful in explaining the irregular variations of the I.S. among neighboring pairs of isotopes of a given element. In light of the new and more precise data being provided by both muonic and electronic x-ray I.S., further attempts at microscopic nuclear calculations would be desirable. More precise calculations of some of the x-ray I.S. atomic coupling effects such as nuclear polarization, screening effects, and the magnetic moment interaction would also be of value.

APPENDIX

Uncorrected Shift Data

As described in Section IV, the data were organized into standard blocs, each of which yielded a single shift value. In Tables 11a - e the shift values for the individual blocs are listed along with the mean shift for each of the five experiments. The uncertainty given is the standard deviation of the mean. The individual shift values are plotted in Figure 12 vs. run number.

TABLE 11a

Run Number	Uncorrected Sn 116-124 Shift (Screw Divisions)	Run Number	Uncorrected Sn 116-124 Shift (Screw Divisions)
1	0.58258	46	0.46891
2	0.33351	47	0.09868
3	0.51610	48	0.13902
4	0.48111	49	0.50378
5	0.75816	50	0.61921
6	0.47327	51	0.70664
7	0.45830	52	0.31504
8	0.68071	53	0.61167
9	0.57024	54	0.58207
10	0.65213	55	0.70656
11	0.55200	56	0.45837
12	0.50582	57	0.38192
13	0.43528	58	0.60966
14	0.29255	59	0.34985
15	0.63228	60	0.51338
16	0.30557	61	0.63165
17	0.60982	62	0.59137
18	0.38446	63	0.77925
19	0.77447	64	0.57613
20	0.85919	65	0.76116
21	0.88720	66	0.17950
22	0.74056	67	0.27335
23	0.36372	68	0.52300
24	0.54201	69	0.42102
25	0.88918	70	0.73965
26	0.75265	71	0.60881
27	0.60717	72	0.73259
28	0.78827	73	0.94527
29	0.61059	74	0.41303
30	0.54802	75	0.56421
31	0.53822	76	0.58349
32	0.42849	77	0.77533
33	0.63938	78	0.52110
34	0.80073	79	0.44995
35	0.52606	80	0.30496
36	0.39552	81	0.63106
37	0.36556	82	0.57623
38	0.78815	83	0.61742
39	0.87425		
40	0.83571		
41	0.93768	Average Shift = + 0.569773 ± 0.020351	
42	0.32360		
43	0.70563		
44	0.80757		
45	0.47337		

TABLE 11b

Run Number	Uncorrected Sm 148-154 Shift (Screw Divisions)	Run Number	Uncorrected Sm 148-154 Shift (Screw Divisions)
1	2.00024	46	1.69273
2	2.19218	47	2.31161
3	1.64372	48	2.51584
4	1.56989	49	2.26780
5	1.89668	50	1.90686
6	2.09317	51	2.52086
7	1.65201	52	1.94864
8	1.88854	53	2.41268
9	2.20409	54	2.18463
10	2.10800	55	2.14173
11	1.93261	56	2.05473
12	2.12880	57	2.18825
13	1.89768	58	2.23301
14	2.45796	59	2.16903
15	1.89827	60	1.90140
16	2.30995	61	1.86709
17	2.19631	62	2.02257
18	1.74537	63	2.24721
19	1.97961	64	1.99236
20	1.82954	65	2.09374
21	2.01454	66	2.05666
22	2.03831	67	1.86962
23	2.20908	68	2.15766
24	2.04515	69	2.24601
25	1.84491	70	1.95870
26	2.10512	71	1.88742
27	1.99377	72	2.06544
28	2.42670	73	2.02557
29	1.86268	74	2.14472
30	2.14875	75	2.09111
31	1.95178	76	2.19923
32	2.22328	77	2.40533
33	2.29737		
34	2.09550		
35	1.85941		
36	2.07499		
37	2.14482		
38	2.01700		
39	2.22866		
40	1.87865		
41	2.05709		
42	1.89563		
43	1.80917		
44	2.13618		
45	1.77342		

Average Shift = 2.058919 ± 0.022910

TABLE 11c

Run Number	Uncorrected W 182-184 Shift (Screw Divisions)	Run Number	Uncorrected W 182-184 Shift (Screw Divisions)
1	-0.38640	46	0.43595
2	0.25415	47	0.24670
3	0.57106	48	0.96253
4	0.21349	49	0.69126
5	0.24604	50	0.39599
6	0.40838	51	0.45451
7	0.99640	52	-0.05966
8	0.02062	53	0.60344
9	0.00431	54	0.41759
10	0.09484	55	-0.07212
11	0.17979	56	0.33973
12	-0.32713	57	0.55203
13	0.38092	58	-0.07716
14	0.29012	59	0.26187
15	0.27253	60	0.61978
16	1.18166	61	0.17481
17	-0.08915	62	0.55560
18	0.78188	63	0.07542
19	0.16811	64	-0.29913
20	0.17674	65	0.87681
21	-0.58338	66	0.63076
22	0.21692	67	0.95488
23	0.19416	68	0.16359
24	0.21852	69	0.36731
25	0.52847	70	0.48341
26	0.46034	71	0.17541
27	0.38783	72	0.41090
28	-0.25783	73	0.33365
29	0.74526	74	0.11138
30	-0.05647	75	0.42394
31	0.40806	76	0.65791
32	0.15074	77	0.35026
33	-0.11353	78	0.92783
34	-0.25542	79	0.48283
35	0.19696	80	0.16663
36	0.18605	81	0.08823
37	-0.04876		
38	0.18460		
39	0.28384	Average Shift = 0.281013 ± 0.037648	
40	0.49985		
41	-0.22841		
42	0.14132		
43	-0.27961		
44	0.27446		
45	0.18487		

TABLE 11d

Run Number	Uncorrected W 184-186 Shift (Screw Divisions)	Run Number	Uncorrected W 184-186 Shift (Screw Divisions)
1	-0.29292	41	0.48213
2	0.16378	42	0.22681
3	-0.39760	43	0.85773
4	0.42643	44	-0.08287
5	0.05047	45	0.45875
6	0.06374	46	-0.26777
7	0.30857	47	-0.28558
8	0.22261	48	-0.19625
9	0.95003	49	0.04162
10	0.17113	50	-0.08626
11	0.28843	51	0.37875
12	0.01075	52	0.09853
13	-0.65334	53	0.10115
14	0.23460	54	0.29319
15	0.12652	55	-0.40247
16	0.14497	56	0.93967
17	-0.35483	57	0.50289
18	0.05008	58	-0.12264
19	0.08448	59	0.08470
20	-0.06543	60	0.90611
21	0.02781	61	0.02722
22	0.05534	62	0.21833
23	-0.26083	63	0.87714
24	0.35258	64	0.19722
25	0.80411	65	0.07270
26	0.29146	66	0.66194
27	-0.38577	67	0.69428
28	-0.15470	68	0.27282
29	-0.02530	69	0.59732
30	-0.46555	70	0.10767
31	-0.55396	71	-0.14432
32	-0.23147	72	0.68085
33	-0.13336	73	0.46280
34	0.60691	74	0.42195
35	-0.17041	75	0.34375
36	0.47328	76	0.47896
37	1.12211	77	0.37782
38	-0.02738	78	0.10954
39	0.51459	79	0.13324
40	-0.13101	80	0.53613

TABLE 11d
Cont.

Run Number	Uncorrected W 184-186 Shift (Screw Divisions)
81	0.15969
82	0.08176
83	0.26991
84	0.02621
85	-0.35136
86	0.21704
87	-0.00199
88	-0.43750
89	0.02811
90	0.22079
91	0.43941
92	-0.20014
93	0.05416
94	-0.19837
95	0.41151
96	0.41931
97	0.10557
98	0.26693
99	0.49462
100	-0.27563
101	0.40678
102	0.66701
103	-0.05786
104	0.43617
105	0.24466
106	0.30384
107	0.33578
108	0.14191
109	0.05973
110	0.13768
111	0.41971
112	0.06722
113	0.36957
114	-0.10653
115	0.10389
116	-0.23640
117	0.19783
118	0.09918
119	0.40941
120	0.79194
121	-0.17248
122	0.21055
123	-0.08777
124	0.75692
125	0.61668
126	0.04220
127	0.48957
128	0.38928
129	0.02546
130	0.28217
131	0.60046
132	0.32853
133	0.42026
134	0.50350
135	0.10350

Average Shift = 0.187606 ± 0.029207

TABLE 11e

Run Number	Uncorrected W 182-186 Shift (Screw Divisions)	Run Number	Uncorrected W 182-186 Shift (Screw Divisions)
1	0.15355	41	0.71031
2	-0.24159	42	0.26777
3	0.42148	43	1.00805
4	0.19582	44	0.76257
5	0.27039	45	0.73158
6	0.66054	46	0.43448
7	0.62824	47	0.36703
8	0.64702	48	1.05464
9	0.57163	49	-0.16619
10	0.40123	50	0.60258
11	0.66539	51	-0.09605
12	1.18765	52	-0.00202
13	-0.18401	53	0.90585
14	0.25730	54	0.51503
15	0.28225	55	0.45492
16	0.22054	56	0.15326
17	0.80341	57	0.18400
18	0.13200	58	0.34485
19	0.35980	59	0.42391
20	0.17674	60	0.15584
21	-0.04728	61	1.30388
22	1.25846	62	0.57426
23	0.70341	63	0.18289
24	0.34494	64	1.22719
25	0.28554	65	0.76124
26	0.31698	66	-0.18497
27	0.62378	67	0.09119
28	0.61248	68	0.50403
29	0.12811	69	0.10629
30	0.03618	70	0.37776
31	0.57658	71	0.11437
32	0.53986	72	0.99064
33	0.17481	73	0.65886
34	1.04385	74	0.88791
35	0.84680	75	0.56552
36	1.09498	76	-0.12125
37	0.75041	77	0.14215
38	0.37299	78	-0.16022
39	0.43427	79	0.71874
40	0.42474	80	0.45365

TABLE 11e
Cont.

Run Number	Uncorrected W 182-186 Shift (Screw Divisions)	Run Number	Uncorrected W 182-186 Shift (Screw Divisions)
81	1.13937	92	0.83071
82	0.60300	93	0.60050
83	0.06067	94	0.48433
84	0.43474	95	0.39952
85	0.82749	96	0.72703
86	0.29875	97	0.60593
87	1.00618	98	0.17665
88	0.63928	99	0.65399
89	0.63425	100	0.10078
90	0.21001	101	0.90080
91	0.72183		

Average Shift = 0.477165 ± 0.035443

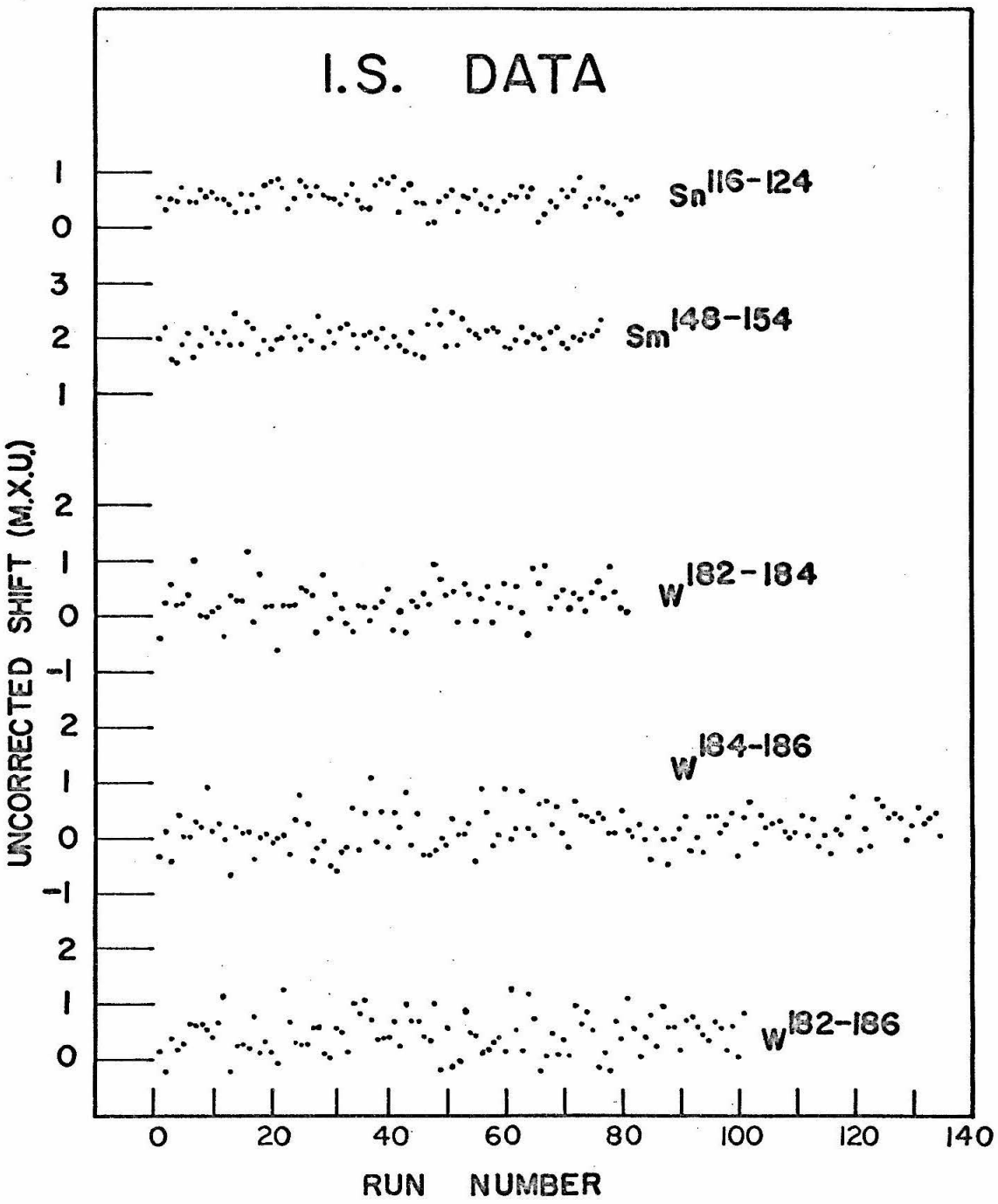
I.S. DATA
Sn116-124
Sm148-154
W182-184
W184-186
W182-186
UNCORRECTED SHIFT (M.X.U.)
RUN NUMBER
0
20
40
60
80
100
120
140

Figure 12

REFERENCES

1) T. R. Merton, Nature 104, 406 (1919).

2) J. H. Bartlett, Nature 128, 408 (1931).

W. Pauli and R. E. Peierls, Phys. Z. 32, 670 (1931).

G. Racah, Nature 129, 723 (1932).

G. Breit, Phys. Rev. 42, 348 (1932).

3) D. N. Stacey, Rep. Progr. Phys. XXIX, 171 (1966).

4) F. K. Richtmyer and S. W. Barnes, Phys. Rev. 37, 1965 (1931).

J. H. Williams, Phys. Rev. 37, 1431 (1931).

M. Frilley, B. G. Gokhale, and M. Valadares, Compt. Rend. 233, 1183 (1951).

G. L. Rogosa and G. Schwarz, Phys. Rev. 92, 1434 (1953).

5) R. T. Brockmeier and F. Boehm, Phys. Rev. Letters 15, 132 (1965).

6) O. I. Sumbaev and A. F. Mezentsev, Soviet Phys. JETP 22, 323 (1966).

7) O. I. Sumbaev and A. F. Mezentsev, Izv. Akad. Nauk. USSR (to be published).

8) C. S. Wu, Int. Conf. Nucl. Phys., Gatlinburg, Tenn., September 1966.

9) M. S. Wertheim and G. Igo, Phys. Rev. 98, 1 (1955).

10) E. K. Broch, Archiv Math. Naturvid. 48, 25 (1945).

11) A. R. Bodmer, Nucl. Phys. 9, 371 (1958-59).

12) F. A. Babushkin, Optics and Spect. XV, 393 (1963).

13) F. A. Babushkin, Soviet Phys. JETP 17, 1118 (1963).

14) A. Sommerfeld, Z. Physik 118, 295 (1941).

15) J. C. Slater, Phys. Rev. 36, 57 (1930).

16) M. E. Rose, Relativistic Electron Theory (Wiley & Sons, Inc., N.Y., 1961) p. 240.

17) E. E. Fradkin, Soviet Phys. JETP 15, 1550 (1962).

18) F. A. Babushkin, Soviet Phys. JETP 18, 1022 (1964).

19) A. S. Reiner and L. Wilets, Nucl. Phys. 36, 457 (1962).

20) E. J. Konopinski and M. E. Rose, "The Theory of Nuclear β Decay," Alpha, Beta, and Gamma Ray Spectroscopy (North Holland Pub. Co., Amsterdam, 1965), Vol. 2, p. 1360.

21) G. Breit and W. Clendenin, Phys. Rev. 85, 689 (1952).

G. Breit, Rev. Mod. Phys. 30, 507 (1958).

22) D. J. Hughes and C. Eckart, Phys. Rev. 36, 694 (1930).

23) F. Herman and S. Skillman, Atomic Structure Calculations(Prentice-Hall, Inc., Inglewood Cliffs, N. J., 1963).

24) J. P. Vinti, Phys. Rev. 56, 1120 (1939).

25) J. C. Slater, Phys. Rev. 38, 1109 (1931).

26) N. Kroll and W. Lamb, Phys. Rev. 75, 388 (1949).

27) W. W. Havens, Jr., L. J. Rainwater, and I. I. Rabi, Phys. Rev. 82, 345 (1951).

28) L. Wilets and D. Hill, Phys. Rev. 91, 1488 (1953).

29) O. I. Sumbaev and A. F. Mezentsev, Soviet Phys. JETP 21, 295 (1965).

30) R. D. Evans, The Atomic Nucleus (McGraw-Hill, Inc., N.Y., 1955), p. 614.

31) E. J. Seppi, H. Henrikson, F. Boehm, and J. W. M. DuMond, Nucl. Inst. and Meth. 16, 17 (1962).

32) P. Brix and H. Kopfermann, Rev. Mod. Phys. 30, 517 (1958).

33) W. R. Hindmarsh and H. Kuhn, Proc. Phys. Soc. (London) A68, 433 (1955).

34) O. I. Sumbaev, A. F. Mezentsev, V. I. Marushenko, E. V. Petrovich, and A. S. Ryl'nikov, Soviet Phys. JETP 23, 572 (1966).

35) B. G. Gokhale, R. B. Chesler, and F. Boehm, Phys. Rev. Letters (to be published).

36) American Society for Testing and Materials, Powder Diffraction File (1966).

37) C. E. Curtis and J. R. Johnson, J. Am. Ceram. Soc. 40, 15 (1957).

38) T. T. Bardin, R. C. Barrett, R. C. Cohen, S. Devons, D. Hitlin, E. Macagno, C. Nissim-Sabat, J. Rainwater, K. Runge, and C. S. Wu, Phys. Rev. Letters 16, 718 (1966).

39) L. Elton, Nucl. Phys. 5, 173 (1958).

40) L. Wilets, D. Hill, and K. Ford, Phys. Rev. 91, 1488 (1953).

41) N. J. Ionesco-Pallas, Il Nuov. Cim. XV, 323 (1960).

42) D. Yeboah-Amankwah, L. Grodzins, and R. Frankel, Phys. Rev. Letters (to be published).

43) S. Bernow, S. Devons, I. Duerdoth, D. Hitlin, J. W. Kast, E. R. Macagno, J. Rainwater, K. Runge, and C. S. Wu, Phys. Rev. Letters (to be published).

44) G. G. Bunatyan and M. A. Mikulinskii, J. Nucl. Phys. (U.S.S.R.) 1, 38 (1965).

45) A. B. Migdal and A. I. Larkin, Soviet Phys. JETP 18, 717 (1964).

46) A. I. Larkin and A. B. Migdal, Soviet Phys. JETP 17, 1146 (1964).

47) L. D. Landau, Soviet Phys. JETP 8, 70 (1959).

48) R. A. Uher and R. A. Sorenson, Nucl. Phys. 86, 1 (1966).

49) F. G. Perey and J. P. Schiffer, Phys. Rev. Letters 17, 324 (1966).